ACS OMEGA

Open Access

This article is licensed under CC-BY-NC-ND 4.0

http://pubs.acs.org/journal/acsodf

Article

Design and Synthesis of Novel Bioactive Squamolone Derivatives Targeting Carbonic Anhydrase and Acetylcholinesterase Enzymes

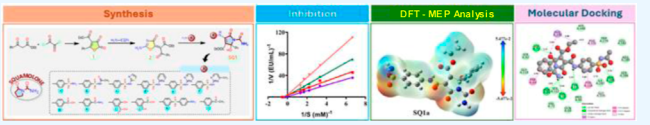
İrfan KOCA,* İrfan ÇAPAN,* Eda Mehtap ÖZDEN, Yusuf SERT, Yeliz DEMİR, and İlhami GÜLÇİN

Cite This: https://doi.org/10.1021/acsomega.6c01815

Read Online

ACCESS | Metrics & More | Article Recommendations | Supporting Information

ABSTRACT: A new series of squamolone-based γ-lactam derivatives (**SQ1a**−**SQ1l**) was rationally designed, synthesized, and structurally confirmed via FT-IR, NMR, and HRMS analyses. The synthesized compounds were evaluated for their inhibitory potential against human carbonic anhydrase isoforms I and II (hCA I and hCA II) and acetylcholinesterase (AChE), enzymes implicated in a range of pathological conditions including glaucoma, epilepsy, cancer, and Alzheimer's disease. Several derivatives demonstrated potent nanomolar inhibition, notably **SQ1g** against hCA I (K_i = 17.99 ± 8.31 nM), **SQ1c** against hCA II (K_i = 31.41 ± 10.26 nM), and **SQ1b** against AChE (K_i = 0.35 ± 0.16 nM). Molecular docking studies corroborated the experimental findings, revealing key hydrogen bonding and hydrophobic interactions within the active sites of each enzyme. Furthermore, DFT-based HOMO−LUMO and molecular electrostatic potential (MEP) analyses provided insight into the compounds' electronic and reactive properties. In silico pharmacokinetic profiling using SwissADME tools showed that several compounds possessed favorable oral bioavailability, lipophilicity, and metabolic stability. Among them, **SQ1g** emerged as the most promising multitarget candidate due to its superior enzymatic activity, drug-like properties, and favorable docking profile. Collectively, these results highlight Squamolone as a versatile pharmacophore for the development of multifunctional enzyme inhibitors with therapeutic potential in neurodegenerative, oncological, and ophthalmological disorders, thereby supporting United Nations Sustainable Development Goal 3 (UN SDG3, Good Health and Well-being) through the advancement of innovative therapeutic agents for major human diseases.



Downloaded via BOZOK UNIV KUT VE DOK on July 3, 2026 at 09:40:44 (UTC).
See https://pubs.acs.org/sharingguidelines for options on how to legitimately share published articles.

1. INTRODUCTION

Carbonic anhydrases (CAs, EC 4.2.1.1) are zinc metalloenzymes that catalyze the reversible hydration of carbon dioxide to bicarbonate and protons, playing a pivotal role in pH homeostasis, ion transport, and biosynthetic processes across tissues.[1,2] Among the 16 known human CA isoforms, hCA I and hCA II are ubiquitously expressed cytosolic isozymes involved in respiratory gas exchange and acid−base balance, with hCA II being the most catalytically active.[3] Aberrant CA activity is implicated in several disorders, including glaucoma, epilepsy, and cancer. In particular, isoforms such as hCA IX and XII are overexpressed in hypoxic tumor microenvironments, where they contribute to extracellular acidosis, tumor progression, and therapeutic resistance.[4] Acetylcholinesterase (AChE), a serine hydrolase responsible for the rapid hydrolysis of acetylcholine at cholinergic synapses, is another validated drug target with major implications in neurodegenerative diseases such as Alzheimer's.[5] Its inhibition elevates synaptic acetylcholine levels, improving cognitive function in patients with cholinergic deficits. AChE possesses a deep and narrow gorge containing both a catalytic active site (CAS) and a peripheral anionic site (PAS), which can be simultaneously targeted by well-designed inhibitors to enhance both potency and disease-modifying effects.[6].

In this context, the development of dual or multitarget enzyme inhibitors remains a compelling strategy in drug discovery. Among privileged scaffolds, γ-lactams (five-membered cyclic amides) have attracted extensive interest due to their broad spectrum of biological activity, conformational rigidity, and synthetic accessibility.[7] This class includes clinically relevant drugs such as cotinine (nicotine metabolite with CNS effects),[8] doxapram (respiratory stimulant),[9] and ethosuximide (T-type calcium channel blocker for absence seizures).[10] Moreover, the racetam family (e.g., piracetam, oxiracetam, aniracetam) exemplifies the neuropharmacological potential of γ-lactam cores in cognitive enhancement and seizure modulation via glutamatergic and calcium-related pathways.[11] Representative γ-lactam-containing drugs are illustrated in Figure 1.

Naturally occurring γ-lactam derivatives further highlight the pharmacological richness of this scaffold. Compounds such as equisetin (an antibiotic and cytotoxic agent from Fusarium species), lactacystin (an irreversible proteasome inhibitor), tenuazonic acid (a protein synthesis inhibitor), and (−)-dysibetaine (a neuroexcitotoxic marine natural product) illustrate their diverse mechanisms of action and therapeutic potential. In addition, pyroglutamic acid, a metabolite involved in glutathione

Received: February 16, 2026
Revised: June 9, 2026
Accepted: June 16, 2026

© XXXX The Authors. Published by American Chemical Society

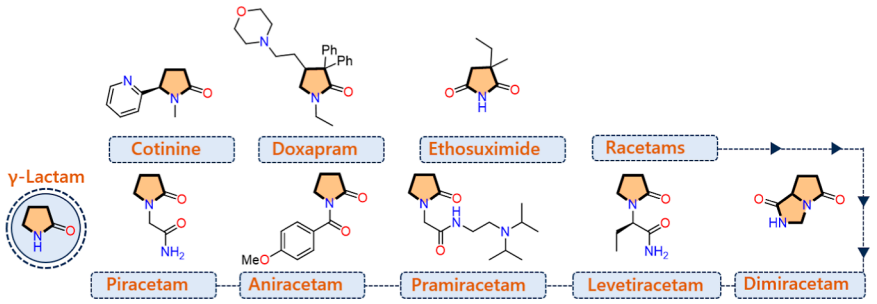


Figure 1. Some drug derivatives containing γ-lactam.

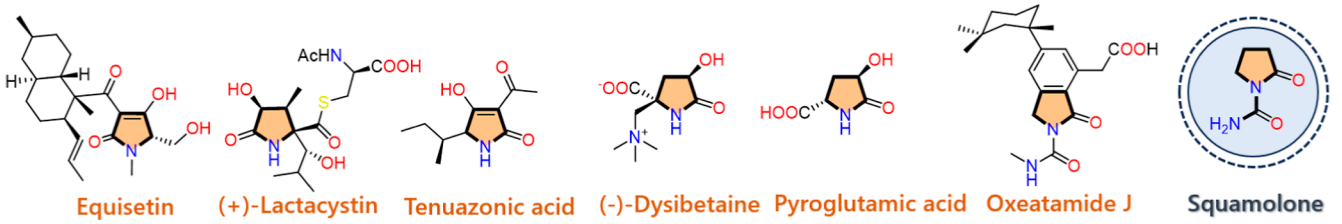


Figure 2. Some natural product derivatives have a γ-lactam structure.

biosynthesis, is a γ-lactam with implications in cognitive modulation and oxidative stress response.[7,12] Selected natural products bearing γ-lactam scaffolds are shown in Figure 2.

Structurally related *N*-acylurea motifs, often found in hydantoin and barbituric acid derivatives, are also widely represented in medicinal chemistry. These include marketed drugs such as phenytoin (antiepileptic), nilutamide (antiandrogen for prostate cancer), and agrochemicals like diflubenzuron (chitin synthesis inhibitor). Their ability to form strong hydrogen bonds and coordinate metal ions underpins their activity against both biological and environmental targets.[13]

Among hybrid natural scaffolds that combine γ-lactam and acylurea features, squamolone, isolated from the fruit of Annona squamosa (custard apple), is particularly noteworthy. Custard apple extracts and squamolone have been associated with anticancer, antioxidant, anti-inflammatory, and analgesic effects.[14] The unique bifunctional structure of squamolone offers multiple interaction points with biological targets, rendering it a highly adaptable pharmacophore in drug design.

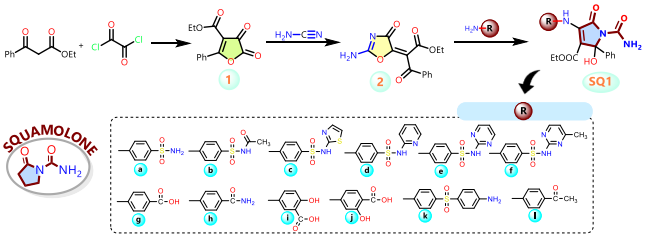
In light of these insights, we report herein the design, synthesis, and biological evaluation of a novel series of squamolone-based derivatives, structurally modified to enhance inhibitory activity against human carbonic anhydrase isoforms (hCA I and II) and acetylcholinesterase. The synthesized compounds were characterized by FT-IR, NMR, and HRMS, and their enzyme inhibitory potential was evaluated through in vitro assays. In addition, molecular docking studies, density functional theory (DFT) analyses, and in silico ADME profiling were performed to elucidate their binding interactions, electronic properties, and pharmacokinetic behavior. This study positions squamolone as a promising core for the development of multifunctional agents targeting both neurodegenerative and oncological pathways.

2. RESULTS AND DISCUSSION

2.1. Chemistry

In the synthetic route toward squamolone-derived scaffolds, 2-aminooxazole (compound **2**) was utilized as a key heterocyclic intermediate. This compound was synthesized from commercially available ethyl benzoylacetate via a previously reported method,[15] forming the oxazole core necessary for downstream derivatization. The target compounds were obtained through nucleophilic substitution reactions of compound **2** with a series of primary and secondary amine derivatives under mild acidic conditions. The reactions were carried out in methanol under reflux for 24 h, in the presence of catalytic acetic acid to facilitate imine formation and subsequent ring closure (Scheme 1).

Scheme 1. Synthesis of Target Compounds



Upon completion of the reaction, the solvent was removed under reduced pressure, and the crude product was precipitated by the addition of cold diethyl ether, affording solid residues. Crude products were subjected to purification either by recrystallization using acetone/diethyl ether (1:2) solvent systems or by flash column chromatography using ethyl acetate/hexane (1:5) as eluents, depending on the polarity and solubility of the specific derivatives. The structural identity and purity of the final squamolone-based compounds (**SQ1a**–**SQ1l**) were confirmed through a comprehensive set of analytical techniques, including FT-IR, ^{1}H NMR, ^{13}C NMR, and high-resolution mass spectrometry (HRMS).

This modular and efficient approach allowed the generation of a diverse library of γ-lactam-acylurea hybrid molecules bearing electronically and sterically distinct substituents, enabling subsequent structure–activity relationship (SAR) analysis against multiple biological targets.

The structure of compound **SQ1a** was thoroughly elucidated using ^{1}H NMR, ^{13}C NMR (APT), FT-IR, and high-resolution mass spectrometry (HRMS) techniques. The ^{1}H NMR

https://doi.org/10.1021/acsomega.6c01815
ACS Omega XXXX, XXX, XXX−XXX

spectrum (600 MHz, DMSO-d_6) displayed a characteristic triplet at δ = 0.70 ppm, corresponding to the terminal methyl protons of the ethyl ester moiety. The methylene protons (−OCH_2−), adjacent to a nonchiral center, appeared as a multiplet at δ = 3.69 ppm, consistent with second-order coupling effects due to the neighboring methyl group. This splitting pattern deviates from the expected quartet, likely due to diastereotopic proton behavior in the absence of symmetry.[16] A broad singlet at δ = 6.94 ppm was assigned to the hydroxyl proton, while the SO_2NH_2 group exhibited a broad singlet at δ = 7.21 ppm, indicative of strong hydrogen bonding and solvent interaction. The urea moiety featured two distinct NH_2 singlets at δ = 7.36 and 7.51 ppm, supporting the presence of a nonequivalent environment for the urea protons. A well-defined singlet at δ = 9.27 ppm was observed for the NH proton at position 3 of the γ-lactam pyrrole ring. The aromatic region (δ = 7.65−7.12 ppm) showed multiple overlapping signals corresponding to nine aromatic protons, fully consistent with the substituted phenyl groups in the molecule. The ^{13}C NMR (APT, 150 MHz, DMSO-d_6) spectrum confirmed the presence of three distinct carbonyl functionalities with signals at δ = 166.4 ppm (ester C═O), 162.2 ppm (lactam C═O), and 150.3 ppm (urea C═O). Signals attributable to the pyrrole ring were observed at δ = 143.8 ppm (C-3), 118.0 ppm (C-4), and 90.8 ppm (C-5). Additional aromatic carbons resonated in the range of δ = 140.6−120.5 ppm. The aliphatic carbons of the ethyl ester chain appeared at δ = 60.2 ppm (OCH_2) and 13.8 ppm (CH_3). High-resolution mass spectrometry (HRMS, ESI) further confirmed the molecular formula of SQ1a as $C_{20}H_{20}N_4O_7S$, with the observed $[M + H]^+$ ion at m/z 461.1114, in excellent agreement with the calculated value of m/z 461.1131.

2.2. Enzyme Inhibition

The sulfonamide group ($-SO_2NH_2$) represents a well-established zinc-binding motif in the design of carbonic anhydrase (CA) inhibitors. This functional group acts as a classical pharmacophore, coordinating with the zinc ion in the active site of CA isoforms and thereby suppressing enzymatic activity via metal chelation and disruption of the proton shuttle mechanism.[2] To systematically explore the influence of structural variation at this pharmacophoric site, a series of *N*-substituted sulfonamide derivatives—such as sulfadiazine and sulfamerazine—were incorporated into the designed molecules as key substituents.

In parallel, bioisosteric replacement strategies were employed to assess how alterations in hydrogen-bonding capacity, polarity, and steric profile affect target binding. Specifically, the SO_2NH_2 group was replaced with carboxamide ($-CONH_2$) moieties, while additional analogs were synthesized bearing carboxylic acid or acetophenone-derived fragments at the same position. These substitutions aimed to probe alternative metal-binding modes, polar interactions, and potential π-stacking effects with the enzyme's active-site residues.

The overall substitution pattern and rational diversification of the aryl and heteroaryl side chains are summarized in Figure 3, which illustrates the modular architecture adopted to generate structure−activity relationship (SAR) insights. The enzyme inhibition results, including IC50, K_i, and correlation coefficient (r^2) values for hCA I, hCA II, and AChE, are presented in Table 1. This strategic scaffold variation provided a focused molecular library enabling differential inhibition across hCA I, hCA II, and AChE, while maintaining a consistent γ-lactam-aryl sulfonamide core.

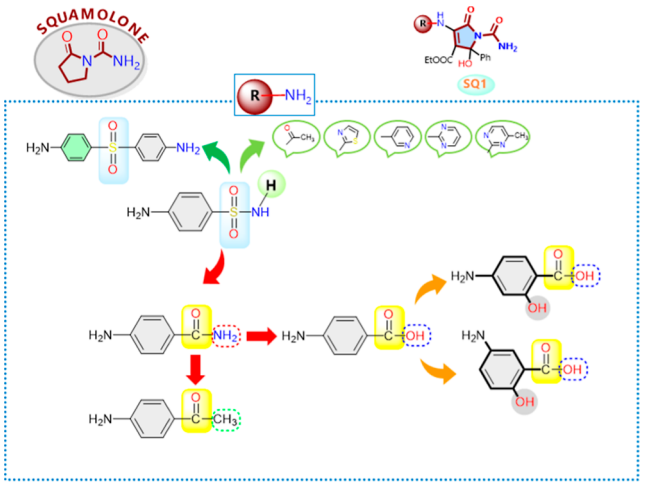


Figure 3. Representative structural modifications introduced at the aniline moiety to explore the impact of various pharmacophores on enzyme inhibition profiles.

The synthesized squamolone-based derivatives (**SQ1a**−**SQ1l**) exhibited a broad spectrum of inhibitory activity against the cytosolic isoform human carbonic anhydrase I (hCA I), with K_i values ranging from 17.99 ± 8.31 nM to 174.08 ± 75.26 nM. For comparison, acetazolamide (AZA), a clinically used CA inhibitor, demonstrated a K_i value of 28.29 ± 6.74 nM under identical assay conditions. Notably, compounds **SQ1g** (K_i = 17.99 ± 8.31 nM), **SQ1c** (K_i = 22.65 ± 9.45 nM), and **SQ1e** (K_i = 24.17 ± 11.90 nM) outperformed AZA in potency, suggesting superior interaction with the hCA I active site. In contrast, **SQ1k**, **SQ1h**, and **SQ1j** displayed K_i values (ranging from 39.76 to 45.85 nM) that were comparable to AZA, whereas **SQ1a** and **SQ1l** were among the least active derivatives.

Among the tested compounds, **SQ1g**, bearing a terminal carboxylic acid moiety, showed the strongest inhibitory profile. This enhancement is attributed to its ability to form electrostatic interactions and potential metal coordination with the zinc-bound water molecule and surrounding polar residues within the active site. Structure−activity relationship (SAR) analysis further revealed that strongly polar, hydrogen-bond-donating substituents, particularly on the sulfonamide or aniline fragments, enhance binding affinity by facilitating anchoring to the zinc-coordinating triad (His94, His96, His119) and hydrophilic pocket residues.

In line with this observation, **SQ1c** and **SQ1e**, functionalized with heterocyclic sulfonamide moieties such as thiazolyl and pyrimidinyl groups, demonstrated notable inhibition. These heteroaryl groups are likely contributing through π−π stacking, dipole−dipole interactions, and enhanced shape complementarity within the enzyme gorge. In contrast, the lower activity of **SQ1l** and **SQ1a** may result from steric hindrance, reduced hydrogen-bonding capacity, or electronic mismatch with key residues in the binding site.

Collectively, these findings emphasize that substitution patterns favoring planarity, polarity, and metal-interactive functionalities are beneficial for achieving potent inhibition against hCA I. These data are visually represented in the Lineweaver−Burk plots shown in Figure 4.

Human carbonic anhydrase II (hCA II) is the most abundant cytosolic isoform and a well-validated therapeutic target, particularly in the treatment of glaucoma, an optic neuropathy characterized by retinal nerve fiber loss and progressive visual

https://doi.org/10.1021/acsomega.6c01815
ACS Omega XXXX, XXX, XXX−XXX

Table 1. Inhibition Constants (K_i) of Squamolone Derivatives against hCAI, hCAII and AChE

Compounds	IC_{50} (nM)						K_i (nM)		
	hCA I	r^2	hCA II	r^2	AChE	r^2	hCA I	hCA II	AChE
SQ1a	46.20	0.9876	33.00	0.9042	2.24	0.9744	174.08±75.26	64.28±20.87	0.78±0.04
SQ1b	28.87	0.9856	53.30	0.9008	2.20	0.9193	97.71±13.8	50.93±14.81	0.35±0.16
SQ1c	53.30	0.9094	36.47	0.9044	3.02	0.9895	22.65±9.45	31.41±10.26	3.73±1.50
SQ1d	53.30	0.9037	36.47	0.9001	2.58	0.9918	52.68±19.17	87.25±31.58	1.71±0.61
SQ1e	46.20	0.9979	33.00	0.9801	2.11	0.9001	24.17±11.90	48.20±23.25	2.70±0.93
SQ1f	38.50	0.9481	57.75	0.9008	2.47	0.9524	80.77±22.46	42.93±13.56	1.65±0.72
SQ1g	46.20	0.9351	69.30	0.9021	2.53	0.9069	17.99±8.31	47.33±15.07	1.66±0.56
SQ1h	36.47	0.9111	57.75	0.9027	3.87	0.9210	41.25±6.42	77.61±37.33	1.51±0.66
SQ1i	34.65	0.9009	57.75	0.9806	3.53	0.9669	70.07±34.47	57.67±25.69	2.22±0.81
SQ1j	28.87	0.9444	53.30	0.9057	5.02	0.9373	45.85±9.59	57.32±21.67	2.13±1.02
SQ1k	24.75	0.9006	34.65	0.9606	2.57	0.9034	39.76±17.44	40.67±19.91	1.00±0.35
SQ1l	46.20	0.9137	77.00	0.9015	4.02	0.9107	131.28±62.97	88.90±14.19	2.87±1.13
Acetazolamide	43.31	0.9922	52.41	0.9775			28.29±6.74	79.75 ±8.34	
Tacrine					13.58	0.9401			53.84±14.83

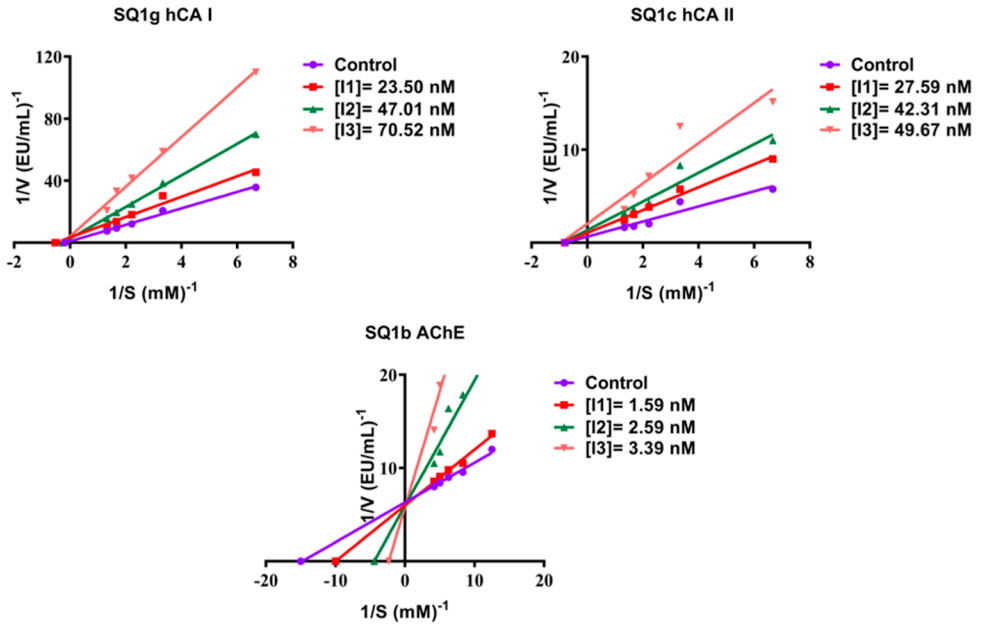


Figure 4. Lineweaver–Burk plots of the compound showing the best inhibition in newly synthesized squamolone derivatives.

field impairment.[17] The elevation of intraocular pressure (IOP), a critical risk factor in glaucoma pathogenesis, is largely driven by the hCA II-catalyzed hydration of CO_2 to bicarbonate and protons.[18] Clinical inhibitors such as acetazolamide (AZA) alleviate IOP by attenuating CA activity and have also been shown to exert vasodilatory effects on retinal arteries.[19]

In this study, squamolone derivatives (**SQ1a–SQ1l**) displayed notable inhibitory activity against hCA II, with K_i values ranging from 31.41 ± 10.26 to 88.90 ± 14.19 nM. Among them, **SQ1c**, incorporating a thiazolyl-sulfamoylphenyl moiety, emerged as the most potent hCA II inhibitor (K_i = 31.41 ± 10.26 nM). The presence of the electron-rich thiazole ring and sulfonamide functionality likely enables $\pi-\pi$ stacking, hydrogen bonding, and favorable electrostatic interactions with the zinc-bound water and nearby polar residues.

Moderate to strong inhibition was observed for **SQ1d**, **SQ1e**, and **SQ1f**, which feature pyridyl or pyrimidinyl substituents. Specifically, **SQ1f** (K_i = 42.93 nM), bearing a methylated pyrimidine, demonstrated enhanced lipophilicity, potentially improving membrane permeability and binding affinity via hydrophobic interactions. Interestingly, **SQ1g** (K_i = 47.33 nM), which lacks a canonical sulfonamide group, showed considerable inhibition, likely due to its benzoic acid moiety mimicking sulfonamide zinc-binding behavior through ionic and hydrogen-bonding interactions.

Compounds **SQ1h–SQ1j**, possessing amide-rich or hydroxy-lated aromatic scaffolds, displayed moderate activity (K_i: 57.32–77.61 nM), possibly limited by inefficient zinc coordination and conformational constraints. The weakest inhibitor, **SQ1l** (K_i = 88.90 nM), features a *p*-acetylphenyl group whose carbonyl

https://doi.org/10.1021/acsomega.6c01815
ACS Omega XXXX, XXX, XXX–XXX

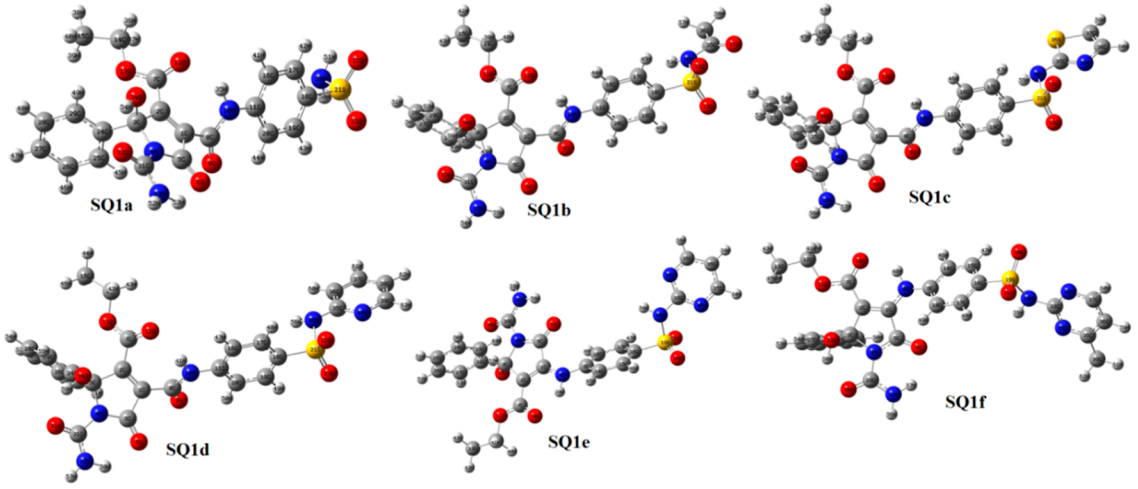


Figure 5. Optimized structures of **SQ1a**-**1f** molecules.

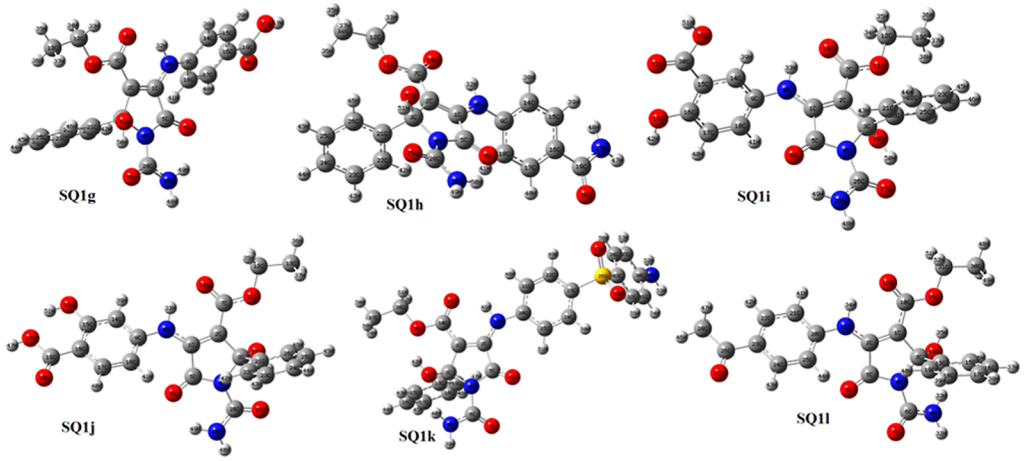


Figure 6. Optimized structures of **SQ1g**-**1l** molecules.

oxygen does not participate effectively in zinc binding and may introduce steric hindrance within the narrow catalytic gorge.

The squamolone derivatives also demonstrated high nanomolar to subnanomolar potency against acetylcholinesterase (AChE), with K_i values ranging from 0.35 ± 0.16 to 3.73 ± 1.24 nM. This variation reflects the influence of C4-aniline substituents on binding orientation and target engagement within the AChE gorge.

The most potent compound, **SQ1b** (K_i = 0.35 ± 0.16 nM), contains an *N*-acetylsulfamoylphenyl fragment, which provides an optimal balance of hydrogen bonding, lipophilicity, and steric bulk. This moiety likely enables simultaneous interaction with both the catalytic active site (CAS) and the peripheral anionic site (PAS) of AChE, a feature highly desirable in multisite inhibitors. Given the exceptionally high inhibitory potency of **SQ1b** against AChE, the inhibition may approach the tight-binding limit under the applied experimental conditions, and the result should therefore be interpreted with appropriate caution while clearly indicating a very strong enzyme−inhibitor interaction. Similarly, **SQ1a** (K_i = 0.78 nM), containing a free 4-sulfamoylphenyl group, validated the classical sulfonamide-AChE interaction model. **SQ1k** (K_i = 1.00 nM) bearing a bisaryl sulfonyl motif terminated by a 4-aminophenyl group, also demonstrated strong activity. Its extended π-conjugation likely facilitates rigid dual-site anchoring, possibly spanning PAS and CAS via aromatic stacking and electrostatic interactions. Compounds **SQ1d**−**SQ1g** (K_i = 1.65−2.70 nM), which carry heteroaryl or carboxyl-substituted phenyl rings, exhibited modest reductions in activity. In **SQ1e** (K_i = 2.70 nM), for example, the unsubstituted pyrimidinyl ring may lack sufficient hydrophobic contact or strong anchoring capacity. However, **SQ1f** (K_i = 1.65 nM), with a 4-methylpyrimidinyl group, gained moderate activity, potentially benefiting from additional van der Waals interactions. **SQ1g**, containing a benzoic acid unit, may participate in polar contacts with gorge residues but might suffer from desolvation penalties or limited passive diffusion. Compounds **SQ1h**−**SQ1j** (K_i = 1.51−2.22 nM), with hydrophilic moieties such as carbamoyl or hydroxylated benzoic acids, maintained moderate potency. However, their interactions likely rely on less favorable solvent-exposed H-bonding, with reduced contribution to enthalpic stabilization or dual-site occupancy.

2.3. DFT Analysis

Density functional theory (DFT)[20] is a powerful method widely used in quantum chemistry to understand and predict the electronic structure of molecular systems. In this study, ligand optimization was performed using the Gaussian 09W package program[21] and the Gaussian 5.0 interface,[22] allowing the determination of the most stable geometric structures. Molecular Electrostatic Potential (MEP) maps were utilized to analyze reactive regions, while molecular orbital calculations

https://doi.org/10.1021/acsomega.6c01815
ACS Omega XXXX, XXX, XXX−XXX

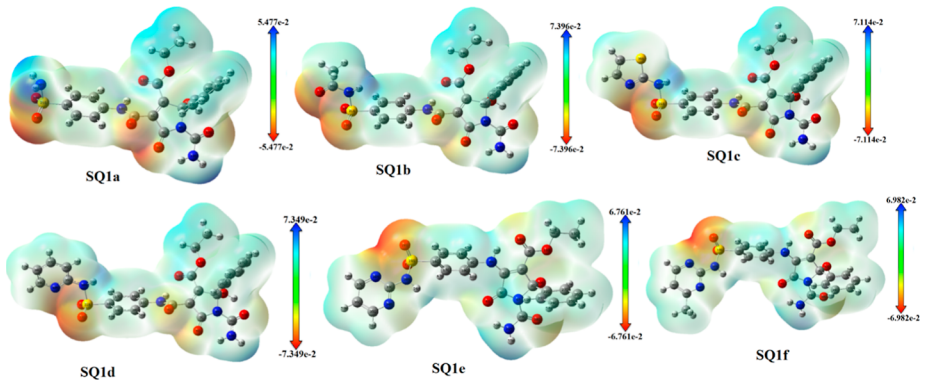


Figure 7. MEP surface of **SQ1a-1f** compounds.

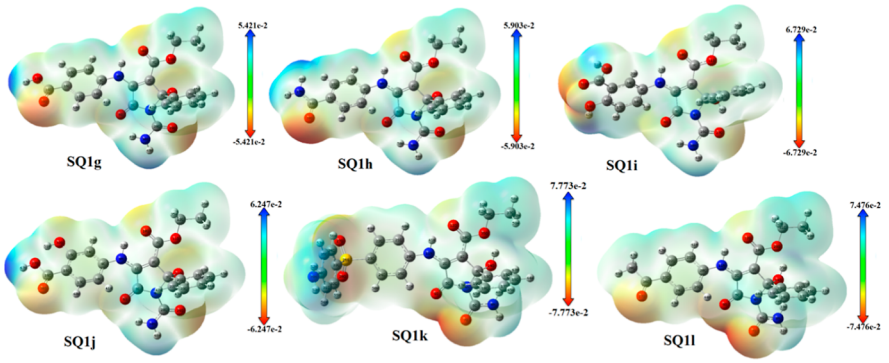


Figure 8. MEP surface of **SQ1g-1l** compounds.

were conducted to determine HOMO−LUMO energy gaps. These calculations provide in-depth insights into the chemical reactivity and interaction mechanisms of target molecules, forming a significant foundation for experimental studies.

2.3.1. Ligand Optimization. The **SQ1a-1l** molecules were optimized in the gas phase using DFT with the B3LYP functional and the 6-311++G(d,p) basis set, implemented in the Gaussian 09W package[21] and visualized using the GaussView 5.0 interface.[22] The optimized structures are presented in Figures 5 and 6. The calculated electronic and zero-point energies for **SQ1a-1l** were determined as −2031.75554506 a.u, −2184.44274604 a.u, −2599.65895322 a.u, −2278.89473289 a.u, −2181.57765778 a.u, −2220.91073848 a.u, −1503.00919229 a.u, −1483.13076452 a.u, −1578.24669696 a.u, −1578.22972776 a.u, −2149.00776739 a.u, and −1467.04802292 a.u, respectively. Based on these energy values, a stability assessment indicates that **SQ1c** exhibits the highest stability among the studied structures.

2.3.2. MEP Analysis. MEP is a key parameter that describes the charge distribution and electrostatic interactions of a molecule with its surroundings. It plays a crucial role in determining the chemical reactivity, biological interactions, and material properties of molecules. In drug design, MEP calculations help predict interactions with target molecules, while in materials science, they aid in understanding and tailoring material properties. MEP surfaces are visualized using a color scale that represents electrostatic potential variations. The color distribution follows the order red < orange < yellow < green < blue, where red indicates regions of negative potential, blue represents positive potential, and green corresponds to neutral regions. This visualization is widely used in fields such as drug design and materials science to analyze and optimize the electrostatic characteristics of molecular surfaces.[23] At this stage of the report, the MEP surfaces of the **SQ1a-1l** molecules were generated based on the optimized structures obtained in the gas phase from the corresponding chk* files. These calculations were performed using DFT with the B3LYP functional and the 6-311++G(d,p) basis set. The MEP analysis allowed the identification of electrophilic (blue) and nucleophilic (red) regions within the molecular structures. The results are presented in Figures 7 and 8. Considering these figures, it can be observed that the electron density is predominantly concentrated around oxygen atoms in all molecules, indicating that these regions correspond to nucleophilic sites. On the other hand, the dark blue regions are localized on hydrogen (H) atoms bonded to oxygen (O) and nitrogen (N) atoms, as well as other hydrogen atoms, signifying electrophilic sites. Furthermore, an analysis of the MEP scales, which provide insight into the electron distribution of the **SQ1a-1l** molecules, reveals that the potential values range as follows: -5.477×10^{-2} to 5.477×10^{-2}, -7.396×10^{-2} to 7.396×10^{-2}, -7.114×10^{-2} to 7.114×10^{-2}, -7.349×10^{-2} to 7.349×10^{-2}, -6.761×10^{-2} to 6.761×10^{-2}, -6.982×10^{-2} to 6.982×10^{-2}, -5.421×10^{-2} to 5.421×10^{-2}, -5.903×10^{-2} to 5.903×10^{-2}, -6.729×10^{-2} to 6.729×10^{-2}, -6.247×10^{-2} to 6.247×10^{-2}, -7.773×10^{-2} to 7.773×10^{-2}, and -7.476×10^{-2} to 7.476×10^{-2}, respectively.

2.3.3. Frontier Orbital Analysis. Frontier molecular orbitals (FMO) theory is essential for understanding molecular reactivity and electronic structure. It classifies orbitals into HOMO (electron-donating) and LUMO (electron-accepting), with their energy gap influencing molecular stability and reactivity. Widely used in organic chemistry, drug design, and materials science, FMO analysis provides key insights into chemical behavior and molecular design.[24] At this stage of the

https://doi.org/10.1021/acsomega.6c01815
ACS Omega XXXX, XXX, XXX−XXX

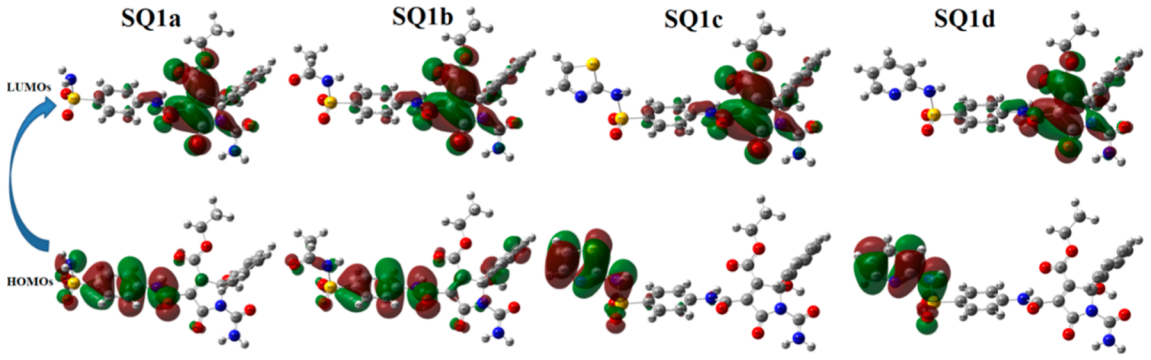


Figure 9. HOMO−LUMO distributions of **SQ1a**−**SQ1d** compounds.

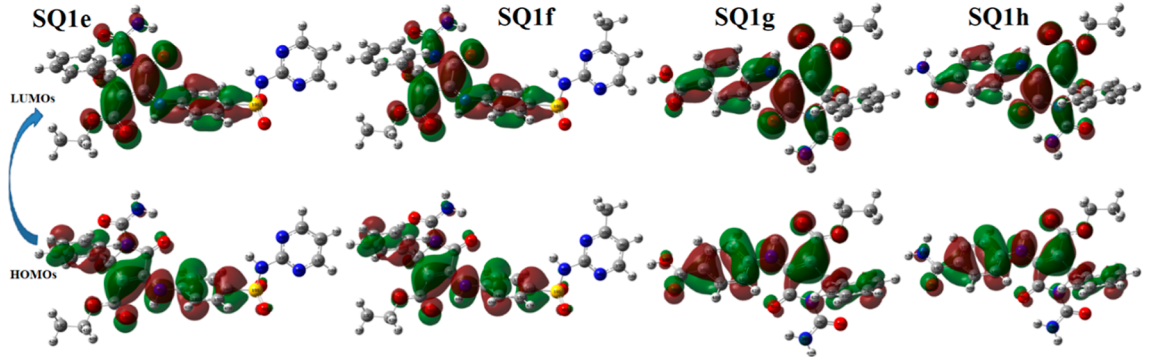


Figure 10. HOMO−LUMO distributions of **SQ1e**−**SQ1h** compounds.

Table 2. Global Descriptors Calculated for SQ1a-1l Molecules in DMF Solution

parameters	SQ1a	SQ1b	SQ1c	SQ1d	SQ1e	SQ1f
E_{LUMO}	−2.686	−2.725	−2.727	−3.105	−2.388	−2.384
E_{HOMO}	−6.587	−6.765	−6.290	−6.781	−6.216	−6.212
energy bandgap $\lvert E_{HOMO} - E_{LUMO}\rvert$	3.901	4.040	3.563	3.676	3.828	3.829
ionization potential $(I = -E_{HOMO})$	6.587	6.765	6.290	6.781	6.216	6.212
electron affinity $(A = -E_{LUMO})$	2.686	2.725	2.727	3.105	2.388	2.384
chemical hardness $(\eta = (I - A)/2)$	1.950	2.020	1.782	1.838	1.914	1.914
chemical softness $(\zeta = 1/2\eta)$	0.256	0.248	0.281	0.272	0.261	0.261
electronegativity $(\chi = (I + A)/2)$	4.636	4.745	4.509	4.943	4.302	4.298
chemical potential $(\mu = -(I + A)/2)$	−4.636	−4.745	−4.509	−4.943	−4.302	−4.298
electrophilicity index $\omega = \mu^2/2\eta$	5.511	5.573	5.706	6.648	4.835	4.825
maximum charge transfer index $(\Delta N_{max.} = -\mu/\eta)$	2.377	2.349	2.531	2.690	2.248	2.245
parameters	SQ1g	SQ1h	SQ1i	SQ1j	SQ1k	SQ1l
E_{LUMO}	−2.367	−2.300	−2.151	−2.377	−2.394	−2.297
E_{HOMO}	−6.067	−6.010	−5.857	−6.060	−5.844	−6.045
energy bandgap $\lvert E_{HOMO} - E_{LUMO}\rvert$	3.700	3.710	3.706	3.683	3.451	3.749
ionization potential $(I = -E_{HOMO})$	6.067	6.010	5.857	6.060	5.844	6.045
electron affinity $(A = -E_{LUMO})$	2.367	2.300	2.151	2.377	2.394	2.297
chemical hardness $(\eta = (I - A)/2)$	1.850	1.855	1.853	1.842	1.725	1.874
chemical softness $(\zeta = 1/2\eta)$	0.270	0.270	0.270	0.271	0.290	0.267
electronegativity $(\chi = (I + A)/2)$	4.217	4.155	4.004	4.219	4.119	4.171
chemical potential $(\mu = -(I + A)/2)$	−4.217	−4.155	−4.004	−4.219	−4.119	−4.171
electrophilicity index $\omega = \mu^2/2\eta$	4.806	4.654	4.325	4.832	4.916	4.641
maximum charge transfer index $(\Delta N_{max.} = -\mu/\eta)$	2.279	2.240	2.160	2.291	2.387	2.225

study, the **SQ1a**-**1l** molecules were first optimized in a dimethylformamide (DMF) solution. Using the chk files obtained from these calculations, the HOMO−LUMO energy values, their spatial distributions, and molecular energy maps were determined. The results are presented in Figures 9−11. Additionally, other key parameters derived from HOMO and LUMO energy values (in eV) were presented in Table 2. These include band gap, ionization potential, electron affinity, chemical hardness, chemical softness, electronegativity, chemical potential, electrophilicity index, and maximum charge transfer index. Based on previous studies in the literature,[25−27] a larger HOMO−LUMO band gap indicates greater molecular stability

https://doi.org/10.1021/acsomega.6c01815
ACS Omega XXXX, XXX, XXX−XXX

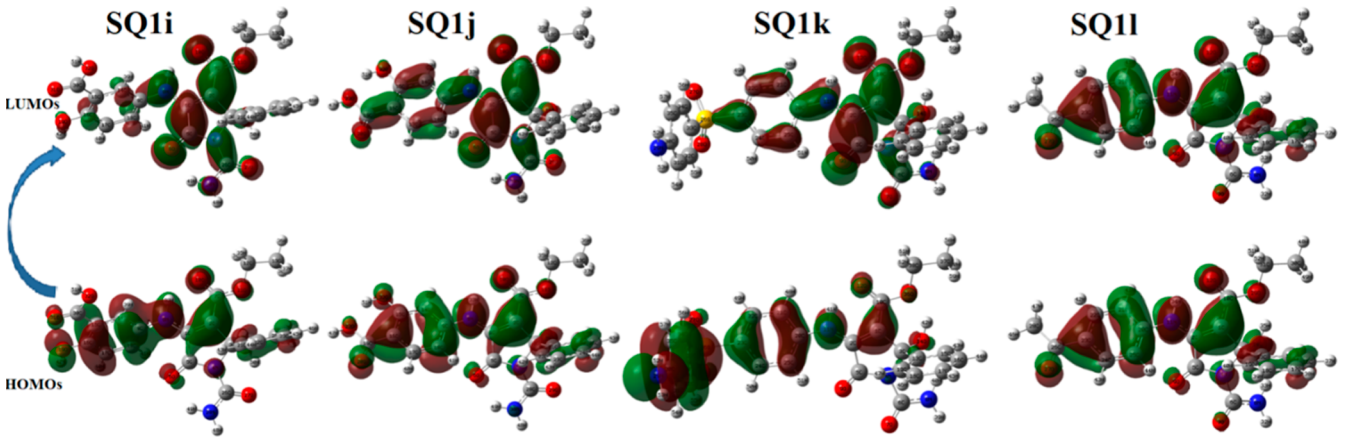


Figure 11. HOMO−LUMO distributions of **SQ1i**−**SQ1l** compounds.

and lower reactivity. Conversely, a smaller band gap enhances chemical reactivity, decreases molecular stability, and lowers the reaction activation energy. As seen in Table 2, the SQ1b molecule exhibits the highest HOMO−LUMO band gap, calculated as 4.040 eV. This suggests that **SQ1b** is more stable and less reactive compared to the other molecules.

The energy ranking follows the order: **SQ1b** > **SQ1a** > **SQ1f** > **SQ1e** > **SQ1l** > **SQ1h** > **SQ1i** > **SQ1g** > **SQ1j** > **SQ1d** > **SQ1c** > **SQ1k**. Based on these results, the **SQ1k** molecule exhibits the highest chemical reactivity, lower stability, and a reduced reaction barrier. The calculations were performed using the IEFPCM solvation model in dimethylformamide (DMF), employing the TD-DFT method with the B3LYP functional and the 6-311++G(d,p) basis set. Ionization energy is defined as the energy required to remove an electron from a molecule in the gas phase[28] and is equal to the negative of the HOMO energy. Conversely, electron affinity represents the energy gained when a gas-phase molecule acquires an additional electron[27] and corresponds to the negative of the LUMO energy. According to the values in Table 2, **SQ1d** exhibits the highest ionization energy and electron affinity. Chemical hardness ($\eta = (I - A)/2$) represents a molecule's resistance to intra- and intermolecular charge transfer,[25] while chemical softness ($\zeta = 1/2\eta$) is its inverse, describing molecules that facilitate charge transfer at relatively lower energy. Based on the values in Table 2, **SQ1b** is identified as the hardest molecule, while SQ1k is the softest. Electronegativity [**33**] describes an atom's ability to attract shared electrons in a chemical bond, whereas chemical potential [**33**] represents a system's response to changes in electron count under a constant external potential. At this point, Table 2 reveals that **SQ1d** exhibits the highest electronegativity and the most negative chemical potential. The electrophilicity index ($\omega = \mu^2/2\eta$)[29] quantifies the decrease in a molecule's total energy during electron transfer between donor and acceptor molecular orbitals. Accordingly, **SQ1d** clearly exhibits the highest electrophilicity index. Finally, considering the maximum charge transfer index ($\Delta N_{max} = -\mu/\eta$), this parameter is used to assess electron transfer processes within a molecule. This index reflects the relationship between the HOMO−LUMO energy gap and the number of double bonds within the molecular structure. A higher value indicates a molecule's greater ability to act as both an electron donor and an electron acceptor.[30] At this point, SQ1d exhibits the highest maximum charge transfer index, while **SQ1i** has the lowest. Based on these evaluations, the distribution of HOMO and LUMO orbitals can be easily examined in Figures 9−11. In Figure 9, for **SQ1a**−**SQ1d**, the HOMO orbitals are predominantly localized on the left side of the molecules, while the LUMO orbitals shift toward the right side and central regions. In contrast, Figure 10 shows that **SQ1e**−**SQ1h** exhibit no significant variation between HOMO and LUMO distributions, a trend that is also observed for **SQ1i**−**SQ1l** in Figure 11. Thus, a notable charge transfer is evident in the first four molecules (**SQ1a**−**SQ1d**). Additionally, these findings provide a foundation for the subsequent section of the study.

2.4. Molecular Docking Study

Molecular docking is a computational modeling approach used to predict the interactions between molecules. This method serves as an effective tool for molecular-level research, enabling the study of how a molecule interacts with other molecules or receptors and predicting the stability of the resulting complexes. Molecular docking finds applications in various fields, including drug design, materials science, chemical reaction mechanisms, biological systems, and protein engineering. In drug design, molecular docking involves identifying the structure of the target molecule, designing and optimizing drug candidates, and analyzing and comparing the resulting complexes. This approach helps predict how drug candidates interact with target receptors and determine which conformations are more stable in terms of energy. In other words, the docking process includes predicting the binding conformation of a ligand to a predicted protein active site and its orientation during binding. Consequently, molecular docking plays a crucial role in accelerating the drug development process and reducing associated costs.[31] A review of the literature reveals that numerous software programs are available for molecular docking However, in this study, we conducted our docking simulations using AutoDock Vina.[32] Developed by Trott and his team in 2010, AutoDock Vina has since played a significant role in various theoretical modeling studies. AutoDock Vina is a computational program designed to calculate and optimize interactions between biomolecules (proteins, DNA, RNA) and small molecules (ligands). Utilizing virtual screening methods, it is widely employed in drug design, molecular modeling, and protein−ligand interaction studies. As an advanced version of the AutoDock program, AutoDock Vina features a more efficient search algorithm and a faster computation engine. Moreover, its user interface is more intuitive, making the program easier to use.

https://doi.org/10.1021/acsomega.6c01815
ACS Omega XXXX, XXX, XXX−XXX

Table 3. Molecular Docking Results for SQ1a-1l Series

	hCA I/PDB: 2CAB (A chain)			hCA II/PDB: 5AML (A chain)			AChE/PDB: 1EVE (A chain)		
entries	binding energies (kcal/mol)	K_i values (nM)	H.B	binding energies (kcal/mol)	K_i values (nM)	H.B	binding energies (kcal/mol)	K_i values (nM)	H.B
SQ1a	−9.2	180.448	6	−9.8	65.5462	3	−12.4	0.814205	5
SQ1b	−9.6	91.8647	6	−9.9	55.3665	3	−12.9	0.350132	5
SQ1c	−10.4	23.8092	5	−10.3	28.1868	3	−11.5	3.71911	4
SQ1d	−9.9	55.3665	5	−9.6	91.8647	2	−11.9	1.189337	4
SQ1e	−10.3	28.1868	6	−10.0	46.7678	3	−11.7	2.65361	4
SQ1f	−9.7	77.5976	3	−10.1	39.5045	3	−11.9	1.89337	4
SQ1g	−10.6	16.988	6	−10.0	46.7678	3	−11.9	1.89337	4
SQ1h	−10.1	39.5045	5	−9.7	77.5976	3	−12.0	1.59932	5
SQ1i	−9.7	77.5976	6	−9.9	55.3665	2	−11.8	2.24149	4
SQ1j	−10.0	46.7678	3	−9.9	55.3665	3	−11.8	2.24149	4
SQ1k	−10.2	33.3692	4	−10.1	39.5045	3	−12.3	0.963905	4
SQ1l	−9.4	128.751	2	−9.6	91.8647	1	−11.7	2.65361	4

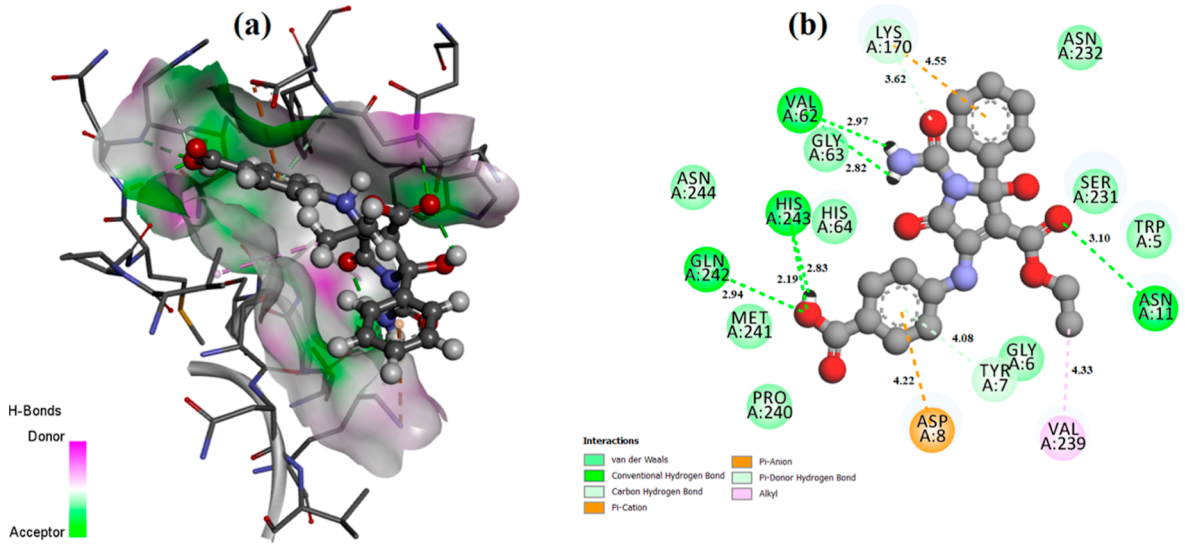


Figure 12. (a) 3D and (b) 2D molecular docking results for the CAI/PDB: 2CAB + SQ1g interaction. The catalytic Zn^{2+} ion was retained during receptor preparation and explicitly considered in all docking calculations; for visual clarity, it is not highlighted in this figure.

To describe the conducted procedures step by step, the initial phase involved optimizing the **SQ1a-1l** molecules in the gas phase. This optimization was performed using the Gaussian 09W software package [25] and the GaussView 5.0 interface [26]. The calculations were carried out within the framework of DFT using the B3LYP functional and the 6-311++G(d, p) basis set. Following optimization, the lowest-energy conformations of the molecules were determined, and the resulting structures were saved in Protein Data Bank (PDB) format. Subsequently, the target structures selected for these molecules were hCAI/PDB: 2CAB,[33,34] hCAII/PDB: 5AML,[34,35] and AChE/PDB: 1EVE.[34,36] The catalytic Zn^{2+} ion present in the active sites of hCA I and hCA II was retained during receptor preparation and explicitly included in all docking calculations. The three-dimensional crystal structures of these targets were obtained from the RCSB PDB.[37] At this stage, the Discovery Studio Visualizer 4.0 (DSV 4.0) software[38] was utilized to prepare the PDBQT files of the ligands by adjusting torsional angles. The catalytic Zn^{2+} ion present in the active site of hCA I and hCA II was retained during receptor preparation and implicitly considered in all docking calculations; its explicit omission in some docking figures reflects a visualization preference rather than exclusion from the computational model.[32,35]

Additionally, this software was used to remove foreign cofactors and water molecules from the receptor proteins under investigation. Before proceeding with the molecular docking process, the active residues of the target proteins were identified. For hCAI/PDB: 2CAB, the active residues were HIS119, HIS96, and HIS94. In the case of hCAII/PDB: 5AML, the identified residues included THR200, THR199, LEU198, PHE131, VAL121, HIS119, HIS96, HIS94, GLN92, ASN67, and ASN62. For AChE/PDB: 1EVE, the active site residues were HIS440, PHE330, GLU327, TRP279, SER200, and TRP84. Thus, the grid parameters for the docking calculations were determined by considering both the active residues and the redocking process. The parameters were set as follows:

- For hCAI/PDB: 2CAB, the grid dimensions were 40 × 40 × 40 $Å^3$ along the *x*, *y*, *z* axes, with a grid spacing of 0.375 Å and center coordinates at (34.428, −10.534, 10.394).
- For hCAII/PDB: 5AML, the grid dimensions were 40 × 40 × 40 $Å^3$, with a grid spacing of 0.375 Å and center coordinates at (−9.799, −1.885, 15.925).
- For AChE/PDB: 1EVE, the grid dimensions were 40 × 40 × 40 $Å^3$, with a grid spacing of 0.375 Å and center coordinates at (5.029, 65.049, 55.8).

https://doi.org/10.1021/acsomega.6c01815
ACS Omega XXXX, XXX, XXX−XXX

Thus, molecular docking of the **SQ1a-1l** ligands with the three selected receptors-hCAI/PDB:2CAB, hCAII/PDB:5AML, and AChE/PDB: 1EVE-was performed using AutoDock Vina. The obtained results are presented in Table 3. As shown in Table 3, the binding energy of each interaction, the corresponding K_i inhibition values, and the number of conventional hydrogen bonds formed during the interactions are provided.

A careful examination of Table 3 reveals that among the interactions between **SQ1a-1l** ligands and the hCAI/PDB: 2CAB receptor, the most favorable ligand was **SQ1g**. Similarly, for the interactions between **SQ1a-1l** ligands and the hCAII/PDB: 5AML receptor, **SQ1c** exhibited the best binding affinity. Lastly, in the case of interactions between **SQ1a-1l** ligands and the AChE/PDB: 1EVE receptor, **SQ1b** was identified as the most favorable ligand. Therefore, the 2D and 3D interaction results, along with the binding sites of the molecules within the respective receptors, were presented in Figures 12−17.

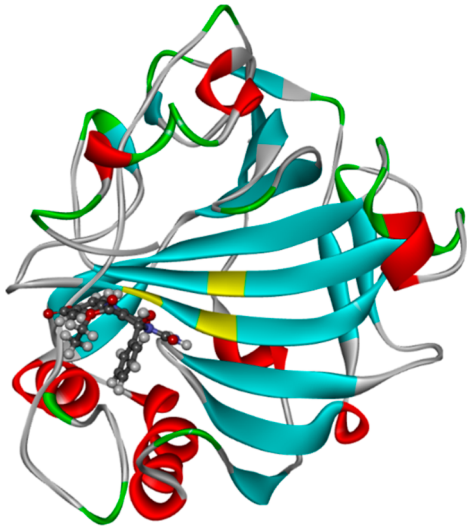


Figure 13. Binding orientation of the SQ1g ligand within the active site of the CAI/PDB: 2CAB receptor. The catalytic Zn^{2+} ion was retained during receptor preparation and explicitly considered in all docking calculations; for visual clarity, it is not highlighted in this figure.

The three-dimensional molecular docking results for the other interactions presented in Table 3 are provided in Figures S49−S81 (Supporting Information). Now, examining the results for each interaction: First, considering the hCAI/PDB: 2CAB + **SQ1a-1l** interactions, it was observed that the most favorable binding occurred in the hCAI/PDB: 2CAB + **SQ1g** complex, with a binding energy of −10.6 kcal/mol. This interaction inhibited the protein with a K_i inhibition constant of 16.988 nM and was stabilized by six hydrogen bonds (Table 3). The 2D interaction diagram (Figure 12b) further illustrates the formation of these six hydrogen bonds, which are as follows:

- VAL62-H48, with a bond length of 2.97 Å,
- VAL62-H49, with a bond length of 2.82 Å,
- HIS243-H47, with a bond length of 2.83 Å,
- HIS243-O27, with a bond length of 2.19 Å,
- GLN242-O27, with a bond length of 2.94 Å,
- ASN11-O10, with a bond length of 3.10 Å.

Additionally, two π-anion/π-cation interactions were identified:

- ASP8 and the center of the phenyl ring, with a bond length of 4.22 Å,
- LYS170 and the center of the phenyl ring, with a bond length of 4.55 Å.

Moreover, two carbon−hydrogen/π-donor hydrogen bond interactions were detected:

- TYR7 and the phenyl ring, with a bond length of 4.08 Å,
- LYS170 and O29, with a bond length of 3.62 Å.

When comparing all interactions in the hCAI/PDB: 2CAB +**SQ1a-1l** complexes based on binding energy, the ranking was determined as follows: **SQ1g** > **SQ1c** > **SQ1e** > **SQ1k** > **SQ1h** > **SQ1j** > **SQ1d** > **SQ1i** = **SQ1f** > **SQ1b** > **SQ1l** > **SQ1a**.

Second, when analyzing the hCAII/PDB: 5AML+**SQ1a-1l** interactions, it was observed that the most favorable binding occurred in the hCAII/PDB: 5AML+**SQ1c** complex, with a binding energy of −10.3 kcal/mol. This interaction inhibited the protein with a K_i inhibition constant of 28.1868 nM and was stabilized by three hydrogen bonds (Table 3). The 2D interaction diagram (Figure 14b) further illustrates the formation of these three hydrogen bonds, which are as follows:

- THR200-O9, with a bond length of 3.07 Å,
- GLN92-O34, with a bond length of 2.71 Å,
- GLN92-O12, with a bond length of 2.83 Å.

Additionally, two $\pi-\pi$ T-shaped interactions were identified:

- HIS94 and the center of the phenyl ring, with a bond length of 5.12 Å,
- HIS64 and the center of the phenyl ring, with a bond length of 4.66 Å.

Moreover, four alkyl/π-alkyl interactions were observed:

- VAL121 and the phenyl ring, with a bond length of 5.16 Å,
- HIS96 and C14, with a bond length of 5.20 Å,
- ALA65 and C14, with a bond length of 3.71 Å,
- LYS170 and the center of the thiazole ring, with a bond length of 5.02 Å.

Lastly, one π-σ interaction was detected between LEU198 and the center of the phenyl ring, with a bond length of 3.57 Å. When comparing all interactions in the hCAII/PDB: 5AML+**SQ1a-1l** complexes based on binding energy, the ranking was determined as follows:

SQ1c > **SQ1f** = **SQ1k** > **SQ1g** = **SQ1e** > **SQ1b** = **SQ1j** = **SQ1i** > **SQ1a** > **SQ1h** > **SQ1d** = **SQ1l**.

The third and final interaction analysis for AChE/PDB: 1EVE + **SQ1a-1l** revealed that the most favorable interaction occurred in the AChE/PDB: 1EVE + **SQ1b** complex, which exhibited a binding energy of −12.9 kcal/mol. This interaction inhibited the protein with a K_i inhibition constant of 0.350132 nM and was stabilized by five hydrogen bonds (Table 3). The 2D interaction diagram (Figure 16b) further illustrates the formation of these five hydrogen bonds, which are as follows:

- ASP172-OH56, with a bond length of 2.01 Å,
- ASN85-H55, with a bond length of 2.81 Å,
- ASN85-H54, with a bond length of 3.04 Å,
- TYR121-H38, with a bond length of 2.25 Å,
- PHE288-O23, with a bond length of 3.30 Å.

Additionally, three $\pi-\pi$ stacked/$\pi-\pi$ T-shaped interactions were observed:

- TRP84 and the center of the phenyl ring, with a bond length of 4.98 Å,

https://doi.org/10.1021/acsomega.6c01815
ACS Omega XXXX, XXX, XXX−XXX

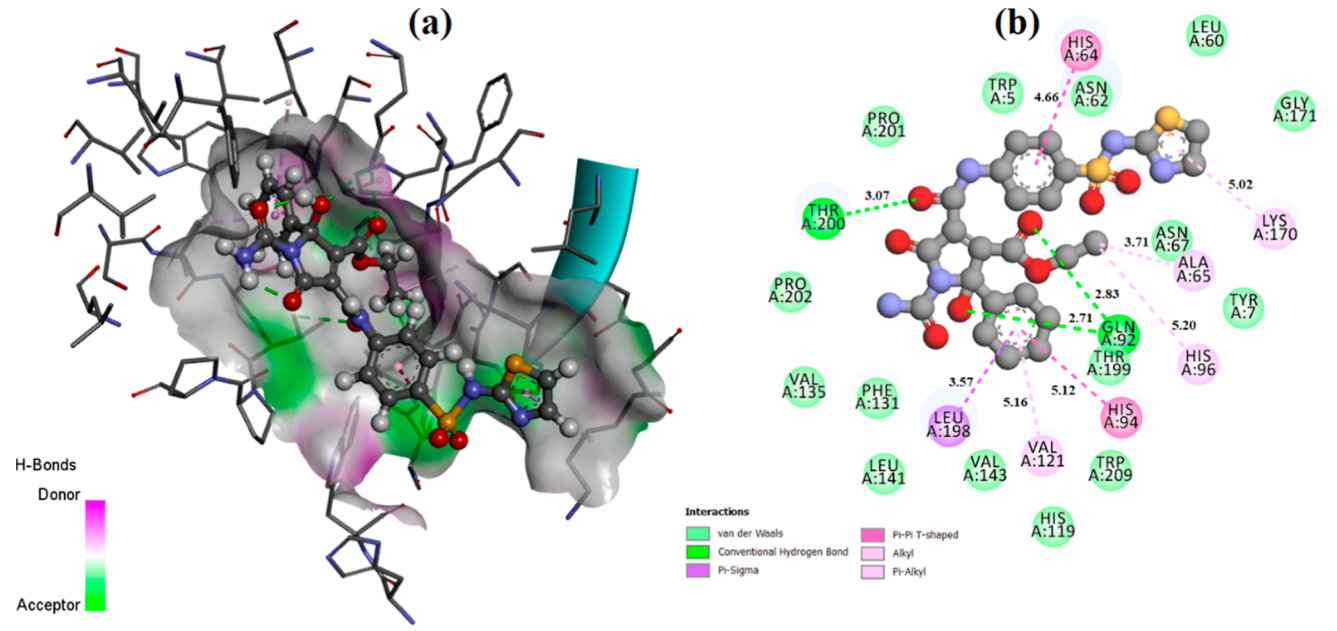


Figure 14. (a) 3D and (b) 2D molecular docking results for the CAII/PDB: 5AML + SQ1c interaction. The catalytic Zn^{2+} ion was retained during receptor preparation and explicitly considered in all docking calculations; for visual clarity, it is not highlighted in this figure.

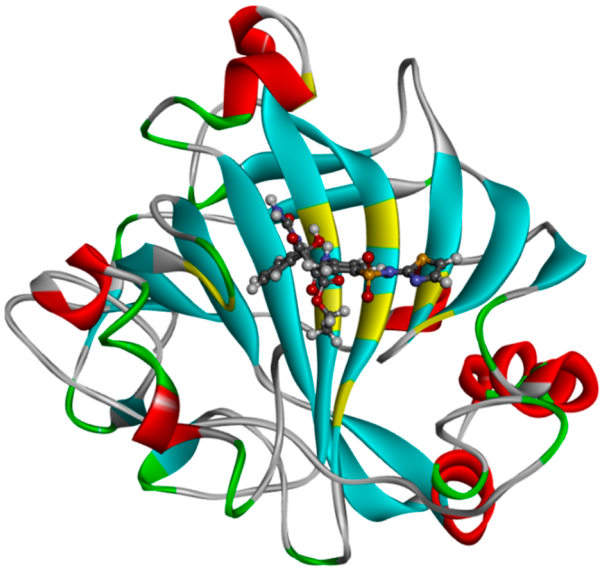


Figure 15. Binding orientation of the SQ1c ligand within the active site of the CAII/PDB: 5AML receptor. The catalytic Zn^{2+} ion was retained during receptor preparation and explicitly considered in all docking calculations; for visual clarity, it is not highlighted in this figure.

- PHE330 and the center of the phenyl ring, with a bond length of 5.66 Å,
- TYR334 and the center of the phenyl ring, with a bond length of 5.85 Å.

Moreover, the following noncovalent interactions were identified:

- One π-alkyl interaction between PHE331 and C15, with a bond length of 4.13 Å,
- One carbon−hydrogen bond interaction between ILE287 and O22, with a bond length of 3.79 Å,
- One π-σ interaction between PHE330 and C15, with a bond length of 3.88 Å.

When comparing all interactions in the AChE/PDB: 1EVE +**SQ1a-1l** complexes based on binding energy, the ranking was determined as follows: **SQ1b** > **SQ1a** > **SQ1k** > **SQ1h** > **SQ1g** = **SQ1f** = **SQ1d** > **SQ1i** = **SQ1j** > **SQ1l** = **SQ1e** > **SQ1c**. The inhibition constants (K_i) presented in Table 3 were calculated using the equation $K_i = \exp^{(\Delta G/RT)}$, where ΔG represents the binding energy, R = 1.987203610^{-3} kcal/(mol·K) is the gas constant, T = 298 K is the temperature. In conclusion, the obtained results indicate that the **SQ1g** molecule effectively inhibits the hCAI/PDB: 2CAB protein, the **SQ1c** molecule exhibits strong inhibition against the hCAII/PDB: 5AML protein, and the **SQ1b** molecule demonstrates significant inhibition of the AChE/PDB: 1EVE protein. Furthermore, when examining the calculated K_i values for each interaction, it is evident that the results are highly consistent with experimental data. This suggests that the selected grid parameters were well-defined and that the docking sites were accurately determined, further validating the reliability of the docking methodology (Figures 13, 15, and 17).

2.5. Drug Likeness and ADME Analysis

In drug discovery, the integration of drug-likeness and ADME (Absorption, Distribution, Metabolism, and Excretion) profiling is essential for identifying compounds with optimal pharmacokinetic behavior and therapeutic potential. These parameters are closely interrelated and are collectively used to predict how a drug will behave in the human body.[39] SwissADME[40] offers a comprehensive computational framework that combines these predictions using intuitive models such as the BOILED-Egg and Bioavailability Radar. The BOILED-Egg model complements this analysis by estimating passive gastrointestinal absorption and brain access based on lipophilicity (WLOGP) and polarity (TPSA), visualized in a two-dimensional plot. These tools, when used in conjunction, not only facilitate the selection of bioavailable and well-distributed compounds but also help eliminate molecules with poor ADME characteristics early in the development pipeline. In parallel, the Bioavailability Radar graphically represents six critical molecular properties-lipophilicity, size, polarity, solubility, flexibility, and saturation-

https://doi.org/10.1021/acsomega.6c01815
ACS Omega XXXX, XXX, XXX−XXX

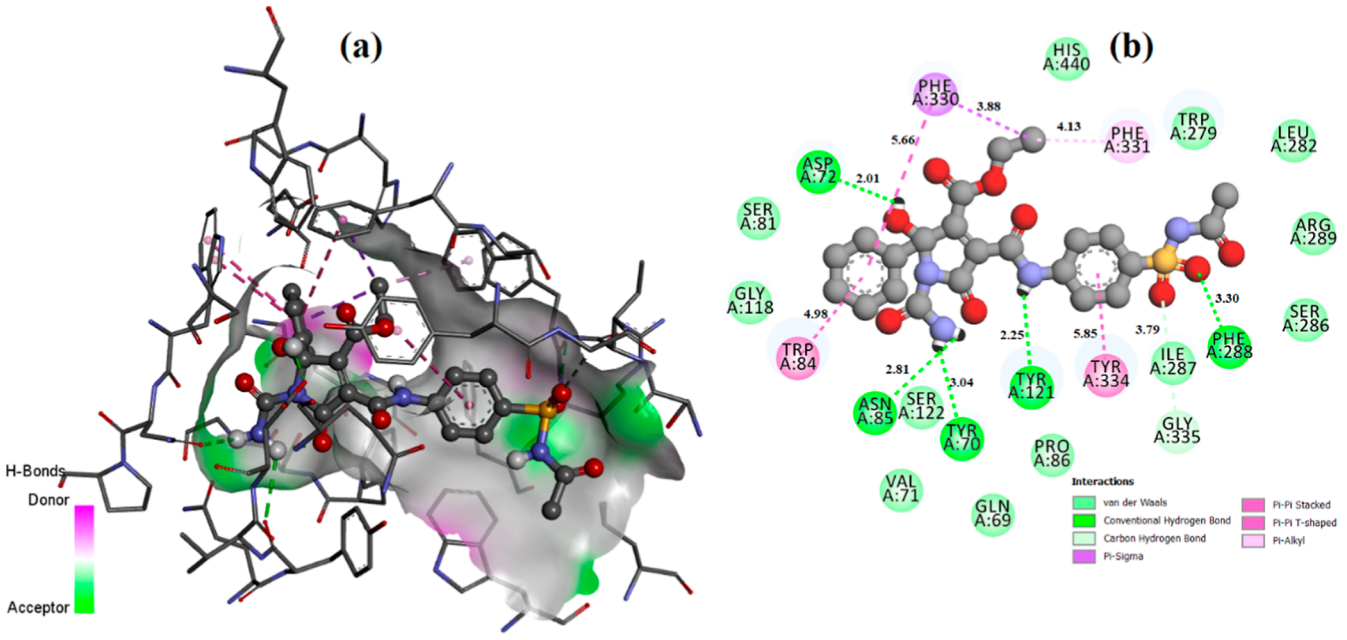


Figure 16. (a) 3D and (b) 2D molecular docking results for the AChE/PDB: 1EVE + SQ1b interaction. Docking calculations were performed using the prepared AChE structure without metal cofactors, consistent with the native catalytic mechanism of acetylcholinesterase.

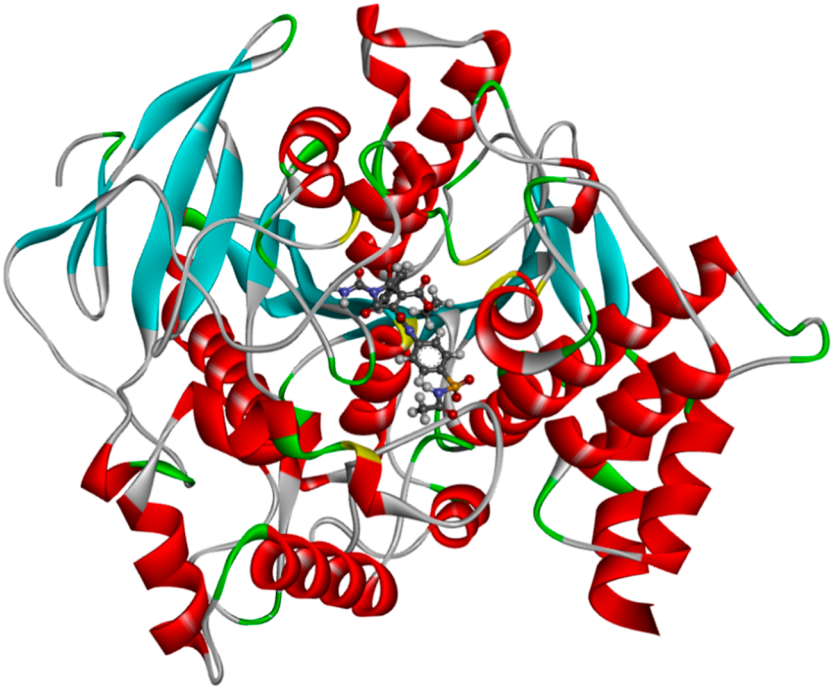


Figure 17. Binding orientation of the SQ1b ligand within the active-site gorge of the AChE/PDB: 1EVE receptor. Ligand−enzyme interactions were evaluated within the catalytic active site and peripheral anionic site regions according to the docking protocol.

allowing for a rapid assessment of oral drug-likeness. A molecule fitting well within the radar's optimal pink area is likely to have favorable oral bioavailability. Thus, by interconnecting drug-likeness evaluation with ADME predictions, the BOILED-Egg and Bioavailability Radar provide a robust, visual, and data-driven strategy for optimizing lead compounds in a rational and time-efficient manner [52]. In line with this literature information, some important physicochemical, lipophilicity properties and pharmacokinetic properties of **SQ1a-1l** molecules produced using SwissADME database were given in Tables 4 and 5, respectively.

Lipinski's rule is used to evaluate the oral bioavailability of compounds based on four criteria: molecular weight ($M_W \leq 500$ Da), hydrogen bond donors (HBD $\leq$ 5), hydrogen bond acceptors (HBA $\leq$ 10), and logP ($\leq$5).[41] Compounds **SQ1b**, **SQ1c**, **SQ1d**, **SQ1e**, **SQ1f**, and **SQ1k** violate two Lipinski rules, mostly due to high molecular weight (>500 Da) and an excessive number of hydrogen bond donors and acceptors (NorO > 10). **SQ1a**, **SQ1i**, and **SQ1j** show only one violation. **SQ1g**, **SQ1h**, and **SQ1l** meet all Lipinski criteria, making them the most drug-like in this series. This suggests that **SQ1g**, **SQ1h**, and **SQ1l** are more promising in terms of oral bioavailability from a rule-based

https://doi.org/10.1021/acsomega.6c01815
ACS Omega XXXX, XXX, XXX−XXX

Table 4. Some Important Physicochemical and Lipophilicity Properties of the SQ1a-1l Series[a]

comp	M_W (g/mol)	nRot	HBA	HBD	TPSA (Å^2)	MR	*M* log *P*	iLOGP	Lipinski rule violation
SQ1a	488.47	9	9	4	207.57	119.93	0.01	1.29	1 (NorO > 10)
SQ1b	530.51	11	9	4	210.65	129.84	−0.38	1.22	2 (MW > 500, NorO > 10)
SQ1c	571.58	11	9	4	234.71	141.73	0.00	2.46	2 (MW > 500, NorO > 10)
SQ1d	565.55	11	9	4	206.47	143.85	0.38	0.78	2 (MW > 500, NorO > 10)
SQ1e	538.53	10	9	4	202.29	136.64	0.03	1.66	2 (MW > 500, NorO > 10)
SQ1f	552.56	10	9	4	202.29	141.60	0.24	1.66	2 (MW > 500, NorO > 10)
SQ1g	425.39	8	7	4	159.26	110.89	0.15	2.20	0
SQ1h	424.41	8	6	4	165.05	112.3	0.85	1.96	0
SQ1i	441.39	8	8	5	179.49	112.92	−0.34	1.82	1 (NorO > 10)
SQ1j	441.39	8	8	5	179.49	112.92	−0.34	1.51	1 (NorO > 10)
SQ1k	536.56	9	7	4	190.5	140.28	1.41	2.51	2 (MW > 500, NorO > 10)
SQ1l	423.42	8	6	3	139.03	114.13	0.76	2.09	0

[a]MW: molecular weight; nRot: Num. Rotable bonds; HBA: Num. H-bond acceptors; HBD: Num. H-bond donors; TPSA: topological polar surface area; MR: molar refractivity; MLOGP: partition coefficient, which measures how hydrophobic (lipophilic); iLOGP: It estimates the energy a molecule needs to transfer from water to octanol.

Table 5. Some Important Pharmacokinetic Properties of the SQ1a-1l Series[a]

comp	GI absorption	BBB permant	*P*-gp substrate	CYP1A2 inhibitor	CYP2C19 inhibitor	CYP2C9 inhibitor	CYP2D6 inhibitor	CYP3A4 inhibitor	log K_p (cm/s)
SQ1a	low	no	yes	no	no	no	no	no	−8.84
SQ1b	low	no	yes	no	no	no	no	no	−8.97
SQ1c	low	no	yes	no	no	no	no	yes	−8.41
SQ1d	low	no	yes	no	no	no	no	no	−8.44
SQ1e	low	no	yes	no	no	no	no	yes	−7.85
SQ1f	low	no	yes	no	no	no	no	yes	−7.65
SQ1g	low	no	yes	no	no	no	no	no	−6.88
SQ1h	low	no	yes	no	no	no	no	no	−7.33
SQ1i	low	no	yes	no	no	no	no	no	−6.84
SQ1j	low	no	yes	no	no	no	no	no	−6.84
SQ1k	low	no	no	no	no	yes	no	yes	−7.14
SQ1l	high	no	yes	no	no	no	no	no	−6.76

[a]GI: gastrointestinal; BBB: blood brain barrier; CYP/cytochrome P450.

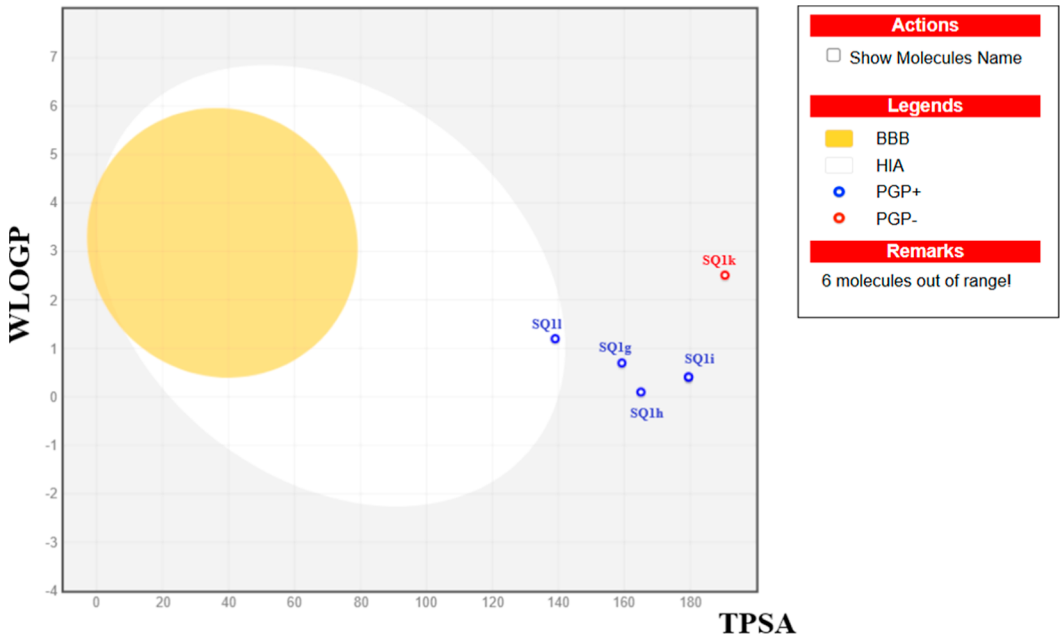


Figure 18. BOILED-EGG graphic of the title molecules.

drug-likeness standpoint (Table 4). Key ADME predictions include gastrointestinal (GI) absorption, blood−brain barrier (BBB) permeability, *P*-glycoprotein (*P*-gp) interaction, cytochrome P450 enzyme inhibition, and skin permeability (Log

https://doi.org/10.1021/acsomega.6c01815
ACS Omega XXXX, XXX, XXX−XXX

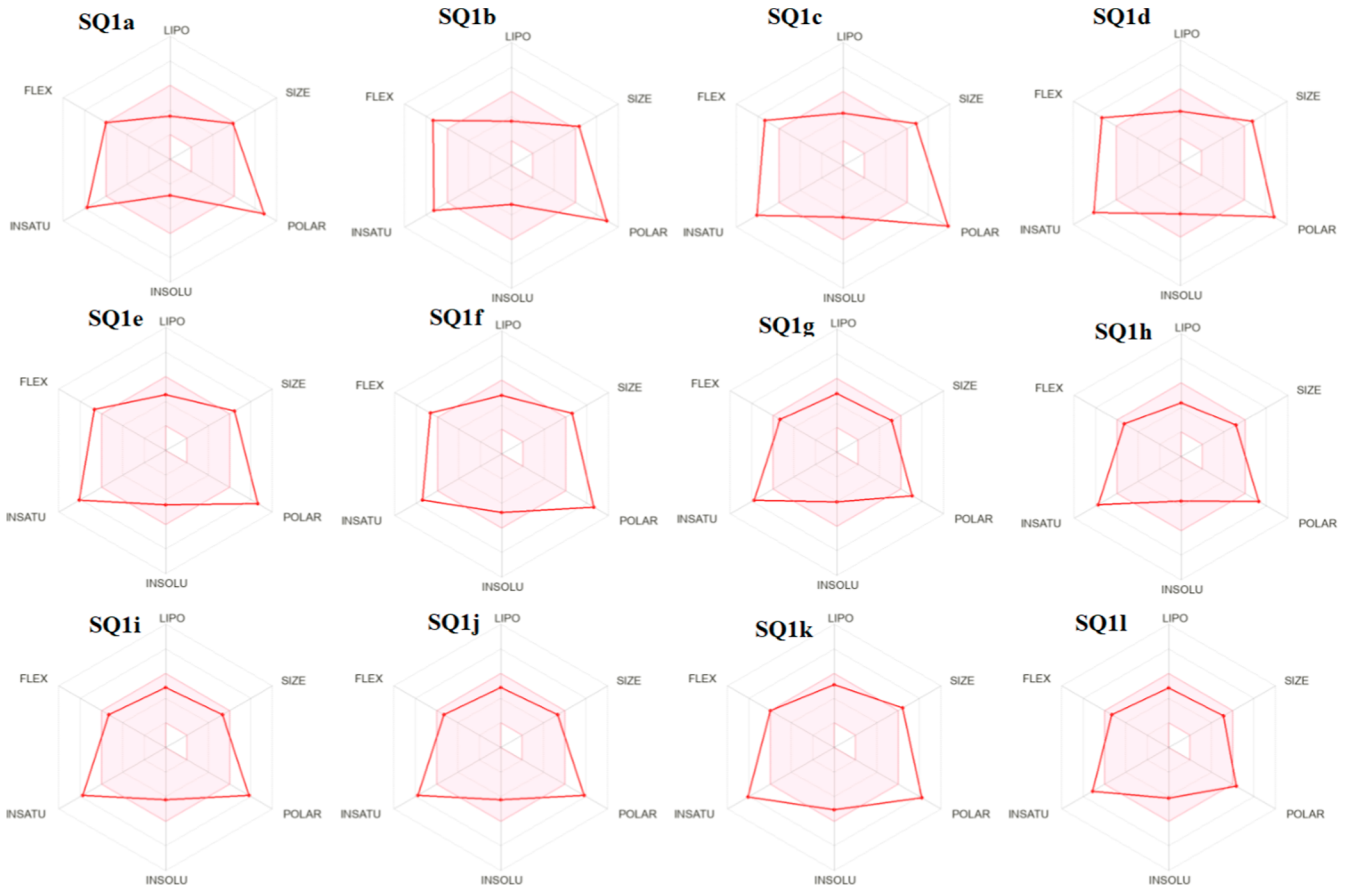


Figure 19. Bioavaibility radars of the title molecules.

K_p). GI absorption is low for almost all molecules except **SQ1l**, which shows high absorption, making it a standout candidate. None of the compounds are predicted to cross the BBB, indicating a low likelihood of CNS side effects-relevant for non-neuroactive drugs. Most compounds are *P*-gp substrates, which may lead to efflux and reduced bioavailability. Enzyme inhibition is minimal across the series, although **SQ1c**, **SQ1e**, **SQ1f**, and **SQ1k** show CYP3A4 inhibition, and **SQ1k** inhibits CYP2C9, suggesting a potential for drug−drug interactions. Log K_p values range from −6.76 to −8.97 cm/s, consistent with moderate to low skin permeability (Table 5). In addition, based on the literature data mentioned above, BOILED EGG and Bioavailability radars of the molecules we are working on are given in Figures 18 and 19 respectively. Accordingly, we can emphasize the following outputs: BOILED-Egg visualization likely shows that SQ1l is the only molecule located in the "white" region, confirming its high GI absorption. The rest fall outside the optimal absorption or BBB permeability zones (Figure 18). Seven of the **SQ1a-1l** molecules are not represented in the BOILED-Egg model (Figure 18) due to their physicochemical properties falling outside the computational boundaries required for BOILED-Egg predictions. Specifically, this model relies on two key parameters: lipophilicity (WLOGP) and topological polar surface area (TPSA). Compounds with extremely high TPSA values (typically >140−150 Å^2) or atypical logP values may fall outside the plotted region of the model. For the excluded molecules, their elevated TPSA-ranging from 202.29 to 234.71 Å^2-likely exceeds the threshold for passive gastrointestinal absorption and blood−brain barrier penetration, making them nonpredictable within the scope of the BOILED-Egg framework. Therefore, these compounds could not be reliably positioned on the diagram and were consequently omitted from Figure 18. Bioavailability Radars for most compounds probably reveal deviations from the ideal physicochemical space (especially in size and polarity), but **SQ1g**, **SQ1h**, and **SQ1l** are expected to have the best radar profiles-falling within the optimal pink zone more consistently (Figure 19).

3. CONCLUSION

In this study, a series of novel squamolone-based hybrid molecules were designed, synthesized, and comprehensively evaluated for their inhibitory potential against pharmacologically relevant enzymes, including human carbonic anhydrase isoforms hCA I and hCA II, and acetylcholinesterase (AChE). The structural framework was rationally engineered by integrating pharmacophoric sulfonamide or bioisosteric carboxamide moieties with electron-rich heterocycles (e.g., thiazole, pyrimidine) onto a squaric acid-derived pyrrole core, aiming to optimize metal coordination, hydrogen bonding, and $\pi-\pi$ stacking interactions within enzyme active sites.

The biological screening revealed that several compounds (notably **SQ1c**, **SQ1g**, and **SQ1b**) demonstrated nanomolar-range inhibition, surpassing or matching clinically used reference inhibitors such as acetazolamide. Structure−activity relationship (SAR) analysis revealed that electronic distribution, hydrogen bond donors/acceptors, and substituent topology at the C4-aniline position significantly influenced enzyme affinity and selectivity. Remarkably, the dual inhibition profile of certain derivatives, such as **SQ1c** and **SQ1f**, suggests their potential as

https://doi.org/10.1021/acsomega.6c01815
ACS Omega XXXX, XXX, XXX−XXX

multitarget-directed ligands (MTDLs) for disorders where both hCA and AChE play pivotal roles, such as glaucoma and neurodegenerative diseases.

In summary, the squamolone derivatives reported herein represent a promising scaffold for the development of multifunctional enzyme inhibitors. Their favorable inhibition profiles, combined with synthetically accessible and modular structures, provide a compelling basis for further preclinical exploration, including in vitro metabolic stability, membrane permeability, and target selectivity assays. These findings underscore the value of scaffold hybridization strategies in medicinal chemistry for generating lead compounds with therapeutic relevance and multifunctional bioactivity.

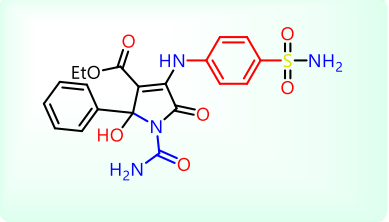
4. EXPERIMENTAL SECTION

4.1. Chemistry

4.1.1. General. All reagents and solvents were purchased from Merck, Fluka, or Sigma-Aldrich and used without further purification unless otherwise stated. Reaction progress and compound purity were monitored by thin-layer chromatography (TLC) on Merck precoated silica gel 60 F254 plates, visualized under UV light at 254 nm. Melting points were determined using an Electrothermal 9200 apparatus and are uncorrected. Infrared spectra (IR) were recorded on a Shimadzu FTIR-8400 spectrometer and are expressed in cm^{-1}. Proton (^1H) and carbon (^{13}C) nuclear magnetic resonance (NMR) spectra were recorded on a Agilent Premium Compact spectrometer operating at 600. MHz, using DMSO-d_6 as solvent. Chemical shifts (δ) are reported in ppm relative to tetramethylsilane (TMS) as the internal standard and coupling constants (J) are given in Hz. Signal multiplicities are designated as s (singlet), d (doublet), t (triplet), dt (doublet of triplets), dd (doublet of doublets), m (multiplet), and br (broad). When necessary, additional NMR experiments, including COSY and APT, were performed for complete spectral assignments.

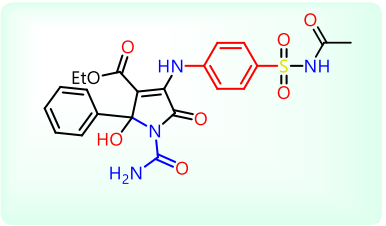
4.1.2. General Procedure for the Preparation of the Target Compounds. A solution of compound 2 (1 mmol) in methanol (30 mL) was heated to reflux until it was completely dissolved. Subsequently, the corresponding amine derivative (1 mmol) and a catalytic amount (one drop) of acetic acid were added, and the reaction mixture was stirred under reflux for 24 h. Upon completion, the solvent was evaporated under reduced pressure, and the resulting oily residue was treated with diethyl ether at room temperature to induce precipitation. The solid was collected by filtration and washed with cold ether. Crude products were purified either by recrystallization from an acetone−diethyl ether (1:2) solvent system or, when necessary, by flash column chromatography using an ethyl acetate−hexane (1:5) solvent mixture as the eluent.

*4.1.2.1. Ethyl 1-Carbamoyl-2-hydroxy-5-oxo-2-phenyl-4-((4-sulfamoylphenyl)amino)-2,5-dihydro-1H-pyrrole-3-carboxylate (**SQ1a**).*



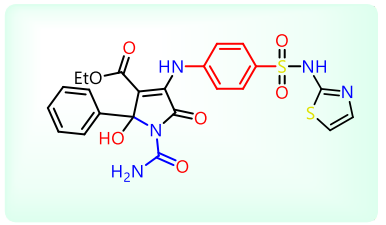
Color: yellow; yields (77%); mp 183 °C. FT-IR (ATR, cm^{-1}): 3421−3287 (NH and OH), 3065 (aromatic CH), 2982 (aliphatic CH), 1736−1634 (C═O), 1592−1474 (aromatic C═C), 1281 (C−O−C).^1H NMR (600 MHz; DMSO-d_6, ppm): δ 9.27 (s, 1H, NH), 7.64 (2H, Part A of AA′BB′ system, Ar−H), 7.51 (br s, 1H, NH), 7.41(d, 2H, J = 7.4 Hz, Ar−H), 7.36 (br s, 1H, NH), 7.26 (t, 2H, J = 7.6 Hz, Ar−H), 7.21−7.18 (m, 3H, NH ve Ar−H), 7.13 (2H, Part B of AA′BB′ system, Ar−H), 6.94 (br s, 1H, OH), 3.75−3.64 (m, 2H, OCH_2), 0.70 (t, 3H, J = 7.4 Hz, CH_3). ^{13}C NMR (150 MHz; DMSO-d_6, ppm): δ 166.4 (CO, ester), 164.2 (CO, lactam), 150.3 (CO, urea), 143.8 (C3, pyrrole), 140.6, 138.4, 137.2, 127.8, 127.5, 126.4, 126.1, 120.5 (Ar C═C), 118.0, (C4, pyrrole), 90.8 (C5, pyrrole), 60.2 (OCH_2), 13.8 (CH_3). HRMS: m/z (M + H) $C_{20}H_{20}N_4O_7S$ calcd, 461.1131; found, 461.1114.

*4.1.2.2. Ethyl 4-((4-(N-acetylsulfamoyl)phenyl)amino)-1-carbamoyl-2-hydroxy-5-oxo-2-phenyl-2,5-dihydro-1H-pyrrole-3-carboxylate (**SQ1b**).*



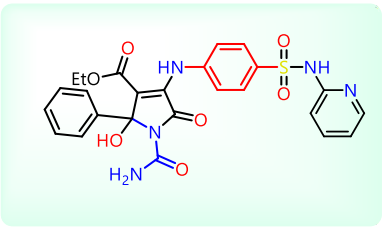
Color: yellow; yields (68%); mp 128 °C. FT-IR (ATR, cm^{-1}): 3421−3200 (NH and OH), 3074 (aromatic CH), 2982 (aliphatic CH), 1729−1640 (C═O), 1590−1450 (aromatic C═C), 1280 (C−O−C). ^1H NMR (600 MHz; DMSO-d_6, ppm): δ 9.38 (s, 1H, NH), 7.76 (2H, Part A of AA′BB′ system, Ar−H), 7.45(d, 2H, J = 7.3 Hz, Ar−H), 7.38 (br s, 1H, NH), 7.30 (t, 2H, J = 7.6 Hz, Ar−H), 7.25−7.22 (m, 3H, NH and Ar−H), 7.17 (2H, Part B of AA′BB′ system, Ar−H), 6.97 (br s, NH), 6.09 (s,1H, OH), 3.75−3.63 (m, 2H, OCH_2), 0.78 (t, 3H, J = 7.3 Hz, CH_3). ^{13}C NMR (150 MHz; DMSO-d_6, ppm): δ 166.8 (CO, amide), 166.5 (CO, ester), 162.0 (CO, lactam), 150.3 (CO, urea), 145.7 (C3, pyrrole), 154.1, 140.4, 136.7, 128.7, 127.9, 126.1, 124.5, 119.9 (Ar C═C), 90.9 (C5, pyrrole), 60.3 (OCH_2), 23.7 (CH_3), 13.7 (CH3). HRMS: m/z (M + H) $C_{22}H_{20}N_2O_8S$ calcd, 503.1237; found, 503.1236.

*4.1.2.3. Ethyl 1-Carbamoyl-2-hydroxy-5-oxo-2-phenyl-4-((4-(N-(thiazol-2-yl)sulfamoyl)phenyl)amino)-2,5-dihydro-1H-pyrrole-3-carboxylate (**SQ1c**).*



Color: yellow; yields (69%); mp 147 °C. FT-IR (ATR, cm^{-1}): 3423−3275 (NH and OH), 3106 (aromatic CH), 2981 (aliphatic CH), 1728−1638 (C═O), 1592−1450 (aromatic C═C), 1277 (C−O−C). ^1H NMR (600 MHz; DMSO-d_6, ppm): δ 9.27 (s, 1H, NH), 7.63 (2H, Part A of AA′BB′ system, Ar−H), 7.51 (br s, 1H, NH), 7.40(m, 2H, Ar−H), 7.39 (br s, 1H, NH), 7.25 (t, 2H, J = 7.7 Hz, Ar−H), 7.20−7.19 (m, 3H, NH and Ar−H), 7.15 (d, 2H, Ar−H, thiazole), 7.09 (2H, Part B of AA′BB′ system, Ar−H), 6.94 (br s, 1H, OH), 6.77 (d,1H, J = 7.7 Hz, Ar−H), 6.77 (d,1H, J = 4.7 Hz, Ar−H), 3.62−3.50 (m, 2H, OCH_2), 0.53 (t, 3H, J = 7.4 Hz, CH_3). ^{13}C NMR (150 MHz; DMSO-d_6, ppm): δ 166.6 (CO, ester), 162.0 (CO, lactam), 150.2 (CO, urea), 144.3 (C3, pyrrole), 152.7, 140.6, 136.8, 136.3, 128.2, 127.8, 127.5, 126.8, 126.0, 120.3, (Ar C═C), 117.9 (C4, pyrrole), 90.9 (C5, pyrrole), 60.1 (OCH_2), 13.4 (CH_3). HRMS: m/z (M + H) $C_{22}H_{20}N_2O_8S$ calcd, 544.0961; found, 544.1006.

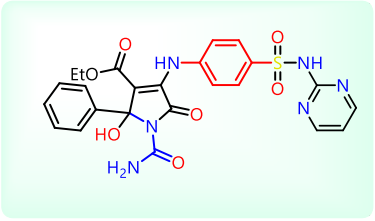
*4.1.2.4. Ethyl 1-Carbamoyl-2-hydroxy-5-oxo-2-phenyl-4-((4-(N-(pyridin-2-yl)sulfamoyl)phenyl)amino)-2,5-dihydro-1H-pyrrole-3-carboxylate (**SQ1d**).*



https://doi.org/10.1021/acsomega.6c01815
ACS Omega XXXX, XXX, XXX−XXX

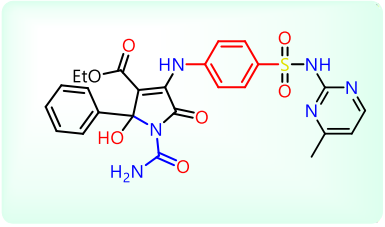
Color: yellow; yields (64%); mp 133−134 °C. FT-IR (ATR, cm^{-1}): 3425−3257 (NH and OH), 3056 (aromatic CH), 2938 (aliphatic CH), 1729−1632 (C═O), 1593−1450 (aromatic C═C), 1271 (C−O−C).^{1}H NMR (600 MHz; DMSO-d_6, ppm): δ 9.28 (s, 1H, NH), 7.72 (2H, Part A of AA′BB′ system, Ar−H), 7.65−6.82(m, 9H, Ar−H), 7.49 (br s, 1H, NH), 7.39 (br s, 1H, NH), 7.07 (2H, Part B of AA′BB′ system, Ar−H), 6.93 (s, 1H, NH), 5.91 (br s, 1H, OH), 3.55−3.42 (m, 2H, OCH_2), 0.46 (t, 3H, J = 7.4 Hz, CH_3). ^{13}C NMR (150 MHz; DMSO-d_6, ppm): δ 166.6 (CO, ester), 161.9 (CO, lactam), 150.2 (CO, urea), 144.6 (C3, pyrrole), 153.2, 152.7, 140.5, 139.1, 136.6, 129.3, 127.9, 127.7, 127.5, 126.0, 120.0, 112.9, 112.5 (Ar C═C), 118.3 (C4, pyrrole), 90.9 (C5, pyrrole), 60.0 (OCH_2), 13.5 (CH_3). HRMS: m/z (M + H)+ $C_{25}H_{23}N_5O_7S$ calcd, 538.1396; found, 538.1339.

*4.1.2.5. Ethyl 1-Carbamoyl-2-hydroxy-5-oxo-2-phenyl-4-((4-(N-(pyrimidin-2-yl)sulfamoyl)phenyl)amino)-2,5-dihydro-1H-pyrrole-3-carboxylate (**SQ1e**).*



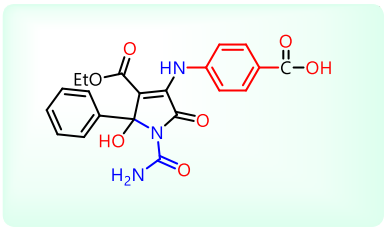
Color: yellow; yields (61%); m.p.: 158 °C. FT-IR (ATR, cm^{-1}): 3432−3249 (NH and OH), 3100 (aromatic CH), 2866 (aliphatic CH), 1728−1631 (C═O), 1591−1453 (aromatic C═C), 1268 (C−O−C).^{1}H NMR (600 MHz; DMSO-d_6, ppm): δ 9.34 (s, 1H, NH), 7.81 (2H, Part A of AA′BB′ system, Ar−H), 8.46−6.99 (m, 8H, Ar−H), 7.50 (br s, 1H, NH), 7.37 (br s, 1H, NH), 7.09 (2H, AA′BB′ system part B, Ar−H), 6.96 (s, 1H, NH), 5.96 (br s, 1H, OH), 3.56−3.44 (m, 2H, OCH_2), 0.43 (t, 3H, J = 7.4 Hz, CH_3). ^{13}C NMR (150 MHz; DMSO-d_6, ppm): δ 166.6 (CO, ester), 161.8 (CO, lactam), 150.2 (CO, urea), 145.3 (C3, pyrrole), 157.7, 157.5, 153.5, 140.4, 136.4, 130.3, 128.8, 127.5, 126.0, 119.7, 112.6 (Ar C═C), 118.8 (C4, pyrrole), 90.9 (C5, pyrrole), 60.0 (OCH2), 13.4 (CH3). HR-MS: m/z (M + H)+ $C_{24}H_{22}N_6O_7S$ calcd, 539.1349; found, 539.1378.

*4.1.2.6. Ethyl 1-Carbamoyl-2-hydroxy-4-((4-(N-(4-methylpyrimidin-2-yl)sulfamoyl)phenyl)amino)-5-oxo-2-phenyl-2,5-dihydro-1H-pyrrole-3-carboxylate (**SQ1f**).*



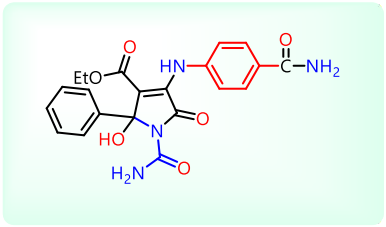
Color: yellow; yields (65%); mp 210 °C. FT-IR (ATR, cm^{-1}): 3423−3277 (NH and OH), 3065 (aromatic CH), 2940 (aliphatic CH), 1730−1625 (C═O), 1584−1467 (aromatic C═C), 1260 (C−O−C).^{1}H NMR (600 MHz; DMSO-d_6, ppm): δ 11.49 (br s, 1H, OH), 9.33 (s, 1H, NH), 7.82 (2H, Part A of AA′BB′ system, Ar−H), 8.28−6.87 (m, 8H, Ar−H), 7.50 (br s, 1H, NH), 7.37 (br s, 1H, NH), 7.10 (2H, Part B of AA′BB′ system, Ar−H), 6.96 (s, 1H, NH), 3.54−3.45 (m, 2H, OCH_2), 2.28 (s, 3H, Ar−CH_3), 0.42 (t, 3H, J = 7.4 Hz, CH_3). ^{13}C NMR (150 MHz; DMSO-d_6, ppm): δ 166.6 (CO, ester), 161.9 (CO, lactam), 150.2 (CO, urea), 145.1 (C3, pyrrole), 157.0, 145.1, 140.4, 136.5, 130.5, 129.0, 127.9, 127.5, 126.0, 119.6, (Ar C═C), 118.7 (C4, pyrrole), 90.9 (C5, pyrrole), 60.0 (OCH_2), 23.7 (Ar−CH_3), 13.4 (CH_3). HRMS: m/z (M + H) $C_{25}H_{24}N_6O_7S$ calcd, 553.151; found, 553.153.

*4.1.2.7. 4-((1-Carbamoyl-4-(ethoxycarbonyl)-5-hydroxy-2-oxo-5-phenyl-2,5-dihydro-1H-pyrrol-3-yl)amino)benzoic Acid (**SQ1g**).*



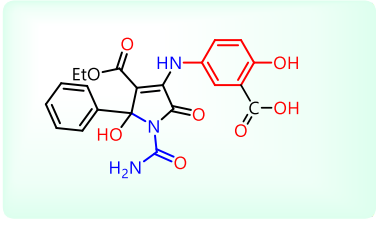
Color: yellow; yields (82%); mp 200 °C. FT-IR (ATR, cm^{-1}): 3418−3256 (NH and OH), 3065 (aromatic CH), 2941 (aliphatic CH), 1751−1636 (C═O), 1600−1447 (aromatic C═C), 1237 (C−O−C). ^{1}H NMR (600 MHz; DMSO-d_6, ppm): δ 12.62 (br s, 1H, OH), 9.27 (s, 1H, NH), 7.78 (2H, Part A of AA′BB′ system, Ar−H), 7.52 (br s, 1H, NH), 7.41 (d, 2H, J = 7.6 Hz, Ar−H), 7.37 (br s, 1H, NH), 7.26 (t, 2H, J = 7.8 Hz, Ar−H), 7.20 (t, 1H, J = 7.3 Hz, Ar−H), 7.06 (2H, Part B of AA′BB′ system, Ar−H), 6.95(s, 1H, NH), 3.72−3.61 (m, 2H, OCH_2), 0.65 (t, 3H, J = 7.4 Hz, CH_3). ^{13}C NMR (150 MHz; DMSO-d_6, ppm): δ 167.4 (CO, c. acid), 166.6 (CO, ester), 162.1 (CO, lactam), 150.3 (CO, urea), 145.1 (C3, pyrrole), 140.6, 136.8, 130.2, 127.9, 127.5, 126.0, 125.0, 119.9 (Ar C═C), 118.3 (C4, pyrrole), 90.9 (C5, pyrrole), 60.1 (OCH_2), 13.7 (CH_3). HRMS: m/z (M + H) $C_{22}H_{19}ClN_2O_4$ calcd, 426.1301; found, 426.1331.

*4.1.2.8. Ethyl 1-Carbamoyl-4-((4-carbamoylphenyl)amino)-2-hydroxy-5-oxo-2-phenyl-2,5-dihydro-1H-pyrrole-3-carboxylate (**SQ1h**).*



Color: yellow; yields (81%); mp 133−134 °C. FT-IR (ATR, cm^{-1}): 3443−3221 (NH and OH), 3059 (aromatic CH), 2866 (aliphatic CH), 1726−1638 (C═O), 1599−1451 (aromatic C═C), 1275 (C−O−C). ^{1}H NMR (600 MHz; DMSO-d_6, ppm): δ 9.16 (s, 1H, NH), 7.80 (br s, 1H, NH), 7.78 (2H, Part A of AA′BB′ system, Ar−H), 7.73 (d, 2H, J = 7.6 Hz, Ar−H), 7.52 (br s, 1H, NH), 7.40 (d, 2H, J = 7.8 Hz, Ar−H), 7.36 (br s, 1H, NH), 7.26 (t, 2H, J = 7.7 Hz, Ar−H), 7.19 (t, 1H, J = 7.3 Hz, Ar−H), 7.03 (2H, Part B of AA′BB′ system, Ar−H), 6.92 (s, 1H, NH), 3.71−3.59 (m, 2H, OCH_2), 0.65 (t, 3H, J = 7.4 Hz, CH_3). ^{13}C NMR (150 MHz; DMSO-d_6, ppm): δ 167.8 (CO, amide), 166.6 (CO, ester), 162.3 (CO, lactam), 150.3 (CO, urea), 144.5 (C3, pyrrole), 140.7, 137.1, 129.5, 128.9, 128.2, 127.8, 126.0, 120.0 (Ar C═C), 117.2 (C4, pyrrole), 90.9 (C5, pyrrole), 60.1 (OCH_2), 13.7 (CH_3). HRMS: m/z (M + H) $C_{21}H_{20}N_4O_6$ calcd, 425.1461; found, 425.1472.

*4.1.2.9. 5-((1-Carbamoyl-4-(ethoxycarbonyl)-5-hydroxy-2-oxo-5-phenyl-2,5-dihydro-1H-pyrrol-3-yl)amino)-2-hydroxybenzoic Acid (**SQ1i**).*

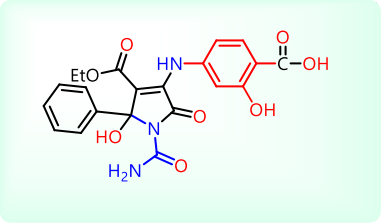


Color: yellow; yields (65%); mp 136 °C. FT-IR (ATR, cm^{-1}): 3455−3290 (NH and OH), 3080 (aromatic CH), 2869 (aliphatic CH), 1738−1631 (C═O), 1596−1441 (aromatic C═C), 1253 (C−O−C). ^{1}H NMR (600 MHz; DMSO-d_6, ppm): δ 11.04 (br s, 1H, OH), 8.88 (s, 1H, NH), 8.45 (br s, 1H, OH), 7.49 (br s, 1H, NH), 7.47−6.85 (m, 7H, Ar−H), 7.32 (br s, 1H, NH), 6.76 (br s, 1H, OH), 3.75−3.62 (m, 2H, OCH_2), 0.74 (t, 3H, J = 7.4 Hz, CH_3). ^{13}C NMR (150 MHz; DMSO-d_6,

https://doi.org/10.1021/acsomega.6c01815
ACS Omega XXXX, XXX, XXX−XXX

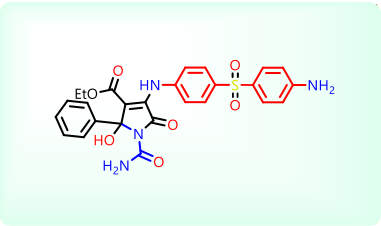
ppm): δ 172.0 (CO, c. acid), 166.3 (CO, ester), 162.7 (CO, lactam), 150.4 (CO, urea), 141.2 (C3, pyrrole), 158.2, 138.8, 132.8, 130.7, 127.7, 127.3, 126.0, 123.8, 117.1, 113.1 (Ar C═C), 112.6 (C4, pyrrole), 90.7 (C5, pyrrole), 59.8 (OCH_2), 13.8 (CH_3). HRMS: *m/z* (M + H) $C_{21}H_{20}N_4O_6$ calcd, 442.125; found, 442.1267.

*4.1.2.10. 4-((1-Carbamoyl-4-(ethoxycarbonyl)-5-hydroxy-2-oxo-5-phenyl-2,5-dihydro-1H-pyrrol-3-yl)amino)-2-hydroxybenzoic Acid (**SQ1j**).*



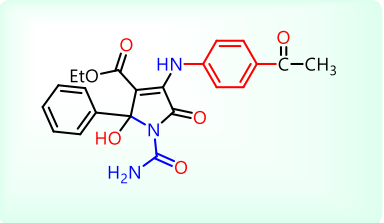
Color: yellow; yields (66%); mp 118 °C. FT-IR (ATR, cm^{-1}): 3421−3249 (NH and OH), 3028 (aromatic CH), 2866 (aliphatic CH), 1730−1637 (C═O), 1613−1450 (aromatic C═C), 1255 (C−O−C). ^1H NMR (500 MHz; DMSO-d_6, ppm): δ 13.5 (br s, 1H, OH), 11.8 (br s, 1H, OH), 8.76 (s, 1H, NH), 7.64−6.99 (m, 8H, Ar−H), 7.54 (br s, 1H, NH), 7.37 (br s, 1H, NH), 6.79 (br s, 1H, OH), 3.78−3.62 (m, 2H, OCH_2), 0.75 (t, 3H, *J* = 7.4 Hz, CH_3). ^{13}C NMR (125 MHz; DMSO-d_6, ppm): δ 172.1 (CO, k. asit), 166.6 (CO, ester), 162.0 (CO, lactam), 150.5 (CO, urea), 147.8 (C3, pyrrole), 158.0, 141.7, 137.8, 136.2, 130.8, 129.3, 127.9, 127.8, 126.0, 11.3 (Ar C═C), 115.3 (C4, pyrrole), 90.9 (C5, pyrrole), 59.9 (OCH_2), 13.8 (CH_3). HRMS: *m/z* (M + H) $C_{21}H_{19}N_3O_8$ calcd, 442.1250; found, 442.1263.

*4.1.2.11. Ethyl 4-((4-((4-aminophenyl)sulfonyl)phenyl)amino)-1-carbamoyl-2-hydroxy-5-oxo-2-phenyl-2,5-dihydro-1H-pyrrole-3-carboxylate (**SQ1k**).*



Color: yellow; yields (48%); mp 148 °C. FT-IR (ATR, cm^{-1}): 3433−3254 (NH and OH), 3062 (aromatic CH), 2939 (aliphatic CH), 1729−1637 (C═O), 1590−1449 (aromatic C═ C), 1279 (C−O−C). ^1H NMR (500 MHz; DMSO-d_6, ppm): δ 9.32 (s, 1H, NH), 7.55 (br s, 1H, NH), 7.70−6.60 (m, 17H, NH and Ar−H), 7.01 (br, s, 1H, OH), 3.70−3.51 (m, 2H, OCH_2), 0.56 (t, 3H, *J* = 7.4 Hz, CH_3). ^{13}C NMR (125 MHz; DMSO-d_6, ppm): δ 166.5 (CO, ester), 162.0 (CO, lactam), 150.3 (CO, urea), 144.9 (C3, pyrrole), 153.8, 140.5, 137.1, 135.3, 129.6, 129.0, 127.9, 127.6, 126.8, 126.1, 120.6, 113.4 (Ar C═C), 118.8 (C4, pyrrole), 90.9 (C5, pyrrole), 60.1 (OCH_2), 13.6 (CH_3). HRMS: *m/z* (M + H) $C_{26}H_{24}N_4O_7S$ calcd, 537.1444; found, 537.1375.

*4.1.2.12. Ethyl 4-((4-acetylphenyl)amino)-1-carbamoyl-2-hydroxy-5-oxo-2-phenyl-2,5-dihydro-1H-pyrrole-3-carboxylate (**SQ1l**).*



Color: yellow; yields (80%); mp 118 °C. FT-IR (ATR, cm^{-1}): 3427−3322 (NH and OH), 3040 (aromatic CH), 2938 (aliphatic CH), 1740−1638 (C═O), 1595−1473 (aromatic C═C), 1268 (C−O−C). ^1H NMR (500 MHz; DMSO-d_6, ppm): δ 9.36 (s, 1H, NH), 7.55 (br s, 1H, NH), 7.85−7.10 (m, 11H, NH and Ar−H), 7.01 (br s, 1H, OH), 3.77−3.66 (m, 2H, OCH_2), 0.70 (t, 3H, *J* = 7.4 Hz, CH_3). ^{13}C NMR (125 MHz; DMSO-d_6, ppm): δ 196.8 (ketone), 166.6 (CO, ester), 162.1 (CO, lactam), 150.3 (CO, urea), 145.5 (C3, pyrrole), 150.2, 140.6, 136.7, 131.6, 129.3, 127.9, 127.6, 119.7 (Ar C═C), 118.9 (C4, pyrrole), 90.9 (C5, pyrrole), 60.2 (OCH_2), 26.9(CH_3), 13.8 (CH_3). HRMS: *m/z* (M + H) $C_{22}H_{21}N_3O_6$ calcd, 424.1509; found, 424.1538.

4.2. Enzyme Inhibition Assay

The in vitro inhibitory activities of the synthesized compounds against hCA I, hCA II and AChE were evaluated using previously established spectrophotometric methods.

4.2.1. CA Inhibition Assay. The inhibitory activities of the compounds against hCA I and hCA II were measured by monitoring the esterase activity of the enzymes using 4-nitrophenyl acetate (4-NPA) as a substrate. The final DMSO concentration did not exceed 1% (v/v). The hydrolysis of 4-NPA was monitored by measuring the absorbance increase at 348 nm due to the formation of 4-nitrophenolate by using Verpoorte's method.[42] The initial velocity data were plotted, and the inhibition constants (K_i values) were calculated by nonlinear regression analysis using the GraphPad Prism software (version 9.0). AZA, a clinically approved CA inhibitor, was used as the positive control.

4.2.2. AChE Inhibition Assay. AChE inhibitory activity was assessed according to Ellman's colorimetric method.[43] The assay mixture contained 0.1 M Tris buffer (pH 8.0), 1 mM 5,5′-dithiobis(2-nitrobenzoic acid) (DTNB), 0.075 U/mL electric eel AChE (Type VI-S, Sigma-Aldrich), and the test compounds. After 15 min of preincubation at room temperature, the reaction was initiated by adding 1 mM acetylthiocholine iodide (AChI). The formation of the yellow 5-thio-2-nitrobenzoate anion, resulting from the reaction between DTNB and thiocholine, was monitored spectrophotometrically at 412 nm for 5 min. Tacrine (THA) was employed as the reference AChE inhibitor for comparative purposes. All measurements were performed in triplicate, and results are reported as means ± standard deviations.

■ ASSOCIATED CONTENT

Supporting Information

The Supporting Information is available free of charge at https://pubs.acs.org/doi/10.1021/acsomega.6c01815.

Synthesis procedures, spectral characterization data (^1H NMR, ^{13}C NMR, FT-IR, HRMS) for all compounds (**SQ1a**−**SQ1l**), additional molecular docking figures (Figures S49−S81), and detailed computational data (DFT, MEP, HOMO−LUMO analyses) (PDF)

■ AUTHOR INFORMATION

Corresponding Authors

İrfan KOCA − *Department of Chemistry, Faculty of Arts and Sciences, Yozgat Bozok University, TR-66900 Yozgat, Turkey*; Phone: +90 354 242 10 21; Email: i_koca@yahoo.com; Fax: +90 354 242 10 22

İrfan ÇAPAN − *Department of Pharmaceutical Basic Sciences, Faculty of Pharmacy, Gazi University, 06330 Ankara, Turkey*; orcid.org/0000-0002-9555-1555; Phone: +90 312 202 3027; Email: irfancapan@gazi.edu.tr; Fax: +90 312 202 80 43

Authors

Eda Mehtap ÖZDEN − *Department of Chemistry, Faculty of Sciences, Atatürk University, 25240 Erzurum, Turkey*

Yusuf SERT − *Sorgun Vocational School, Yozgat Bozok University, 66900 Yozgat, Turkey*

Yeliz DEMİR − *Department of Chemistry, Faculty of Sciences, Atatürk University, 25240 Erzurum, Turkey; Department of*

https://doi.org/10.1021/acsomega.6c01815
ACS Omega XXXX, XXX, XXX−XXX

Pharmacy Services, Nihat Delibalta Göle Vocational High School, Ardahan University, 75700 Ardahan, Turkey

İlhami GÜLÇİN − *Department of Chemistry, Faculty of Sciences, Atatürk University, 25240 Erzurum, Turkey;* orcid.org/0000-0001-5993-1668

Complete contact information is available at: https://pubs.acs.org/10.1021/acsomega.6c01815

Author Contributions

All authors have made essential contributions to this study. Establishing the outline of the study: İK, İG; Synthesis and characterization: İK, İÇ; Biological activity: İG, YD, EMÖ; Theoretical and Molecular Docking studies: YS, İK; Manuscript drafting; İK, YS, YD, İG. All authors read and approved the final manuscript.

Notes

The authors declare no competing financial interest.

■ ACKNOWLEDGMENTS

The authors acknowledge financial assistance from The Scientific and Technological Research Council of Turkey (TÜBİTAK) (Project No: 221Z161) and Yozgat Bozok University Science and Technology Practice & Research Centre (Project No: FED-2026-2313).

■ REFERENCES

(1) Yiğit, B.; Taslimi, P.; Celepci, D. B.; Taskin-Tok, T.; Yiğit, M.; Aygün, M.; Özdemir, I.·.; Gülçin, I.·. Novel PEPPSI-type N-heterocyclic carbene palladium (II) complexes: Synthesis, characterization, in silico studies and enzyme inhibitory properties against some metabolic enzymes. *Inorg. Chim. Acta* **2023**, *544*, 121239.

(2) Supuran, C. T.; Scozzafava, A. Carbonic anhydrase inhibitors. *Curr. Med. Chem.: Immunol., Endocr. Metab. Agents* **2001**, *1* (1), 61−97.

(3) Korkusuz, E.; Sert, Y.; Arslan, S.; Aydın, H.; Yıldırım, I.·.; Demir, Y.; Gülçin, I.·.; Koca, I.·. Synthesis and biological studies of pyrimidine derivatives targeting metabolic enzymes. *Archiv der Pharmazie* **2024**, *357* (8), 2300634.

(4) (a) Supuran, C. T. Emerging role of carbonic anhydrase inhibitors. *Clin. Sci.* **2021**, *135* (10), 1233−1249. (b) M. Monti, S.; T. Supuran, C.; De Simone, G. Carbonic anhydrase IX as a target for designing novel anticancer drugs. *Curr. Med. Chem.* **2012**, *19* (6), 821−830.

(5) Taslimi, P.; Köksal, E.; Gören, A. C.; Bursal, E.; Aras, A.; Kılıç, O.·.; Alwasel, S.; Gülçin, I.·. Anti-Alzheimer, antidiabetic and antioxidant potential of Satureja cuneifolia and analysis of its phenolic contents by LC-MS/MS. *Arabian J. Chem.* **2020**, *13* (3), 4528−4537.

(6) (a) Bal, S.; Kaya, R.; Gök, Y.; Taslimi, P.; Aktaş, A.; Karaman, M.; Gülçin, I. ·. Novel 2-methylimidazolium salts: Synthesis, characterization, molecular docking, and carbonic anhydrase and acetylcholinesterase inhibitory properties. *Bioorg. Chem.* **2020**, *94*, 103468. (b) Bayrak, C.¸.; Taslimi, P.; Gülçin, I.·.; Menzek, A. The first synthesis of 4-phenylbutenone derivative bromophenols including natural products and their inhibition profiles for carbonic anhydrase, acetylcholinesterase and butyrylcholinesterase enzymes. *Bioorg. Chem.* **2017**, *72*, 359−366.

(7) Caruano, J.; Muccioli, G.; Robiette, R. Biologically active γ-lactams: synthesis and natural sources. *Org. Biomol. Chem.* **2016**, *14* (43), 10134−10156.

(8) Etzel, R. A. A review of the use of saliva cotinine as a marker of tobacco smoke exposure. *Prev. Med.* **1990**, *19* (2), 190−197.

(9) Yost, C. S. A new look at the respiratory stimulant doxapram. *CNS Drug Rev.* **2006**, *12* (3−4), 236−249.

(10) Glauser, T. A.; Perucca, E. *Ethosuximide the treatment of epilepsy*, 2015; pp 460−471.

(11) (a) Schifano, F.; Catalani, V.; Sharif, S.; Napoletano, F.; Corkery, J. M.; Arillotta, D.; Fergus, S.; Vento, A.; Guirguis, A. Benefits and harms of 'smart drugs'(nootropics) in healthy individuals. *Drugs* **2022**, *82* (6), 633−647. (b) Mansour, N. M.; El-Sherbiny, D.; Ibrahim, F. A.; El-Subbagh, H. I. Review on bioanalytical and analytical method development of Antiepileptic racetams. *Delta Univ. Scient. J.* **2022**, *5* (2), 53−62.

(12) Nay, B.; Riache, N.; Evanno, L. Chemistry and biology of non-tetramic γ-hydroxy-γ-lactams and γ-alkylidene-γ-lactams from natural sources. *Nat. Prod. Rep.* **2009**, *26* (8), 1044−1062.

(13) Rohilla, J.; Mishra, R.; Varshney, S.; Mazumder, A.; Mazumder, R.; Kumar, A.; Kaur, A. Multi-functional Acyl Urea Compounds: A Review on Related Patents, Clinical Trials, and Synthetic Approaches. *Curr. Org. Chem.* **2024**, *28* (17), 1366−1379.

(14) Nugraha, A. S.; Damayanti, Y. D.; Wangchuk, P.; Keller, P. A. Anti-infective and anti-cancer properties of the Annona species: Their ethnomedicinal uses, alkaloid diversity, and pharmacological activities. *Molecules* **2019**, *24* (23), 4419.

(15) Kibriz, I.·. E.; Saçmaci, M.; Şahin, E.; Yildirim, I. Preparation of novel pyrrol-2-one derivatives via an effective synthesis of new oxazole scaffold. *Tetrahedron* **2017**, *73* (14), 1795−1802.

(16) Balci, M. *Basic 1H-and 13C-NMR spectroscopy*; Elsevier, 2005.

(17) Yu, J.; Zhang, Y.; Kam, K. W.; Ho, M.; Young, A. L.; Pang, C. P.; Tham, C. C.; Yam, J. C.; Chen, L. J. Lung Function as a Biomarker for Glaucoma: The UK Biobank Study. *Invest. Ophthalmol. Visual Sci.* **2025**, *66* (2), 48.

(18) (a) Karagecili, H.; Yılmaz, M. A.; Ertürk, A.; Kiziltas, H.; Güven, L.; Alwasel, S. H.; Gulcin, I.·. Comprehensive metabolite profiling of Berdav propolis using LC-MS/MS: Determination of antioxidant, anticholinergic, antiglaucoma, and antidiabetic effects. *Molecules* **2023**, *28* (4), 1739. (b) Güven, L.; Erturk, A.; Miloğlu, F. D.; Alwasel, S.; Gulcin, İ. Gulcin, İ. Screening of antiglaucoma, antidiabetic, anti-alzheimer, and antioxidant activities of Astragalus alopecurus pall analysis of phenolics profiles by LC-MS/MS. *Pharmaceuticals* **2023**, *16* (5), 659.

(19) Oktay, K.; Köse, L. P.; Şendil, K.; Gültekin, M. S.; Gülçin, I.·.; Supuran, C. T. The synthesis of (Z)-4-oxo-4-(arylamino) but-2-enoic acids derivatives and determination of their inhibition properties against human carbonic anhydrase I and II isoenzymes. *J. Enzyme Inhib. Med. Chem.* **2016**, *31* (6), 939−945.

(20) Eschrig, H. *The fundamentals of density functional theory*; Springer, 1996.

(21) Frisch, M. *Gaussian 09*, Revision d. 01; Gaussian. Inc: Wallingford CT, 2009; Vol. *201*.

(22) Dennington, R.; Keith, T. J. M. *GaussView*. Version, 2009.

(23) (a) Murray, J. S.; Sen, K. *Molecular electrostatic potentials: concepts and applications*, 1996. (b) Weiner, P. K.; Langridge, R.; Blaney, J. M.; Schaefer, R.; Kollman, P. A. Electrostatic potential molecular surfaces. *Proc. Natl. Acad. Sci. U. S. A.* **1982**, *79* (12), 3754−3758. (c) Cox, S.; Williams, a. D. Representation of the molecular electrostatic potential by a net atomic charge model. *J. Comput. Chem.* **1981**, *2* (3), 304−323. (d) Sjoberg, P.; Politzer, P. Use of the electrostatic potential at the molecular surface to interpret and predict nucleophilic processes. *J. Phys. Chem.* **1990**, *94* (10), 3959−3961.

(24) (a) Fukui, K. Role of frontier orbitals in chemical reactions. *science* **1982**, *218* (4574), 747−754. (b) Fukui, K.; Yonezawa, T.; Nagata, C.; Shingu, H. Molecular orbital theory of orientation in aromatic, heteroaromatic, and other conjugated molecules. *J. Chem. Phys.* **1954**, *22* (8), 1433−1442.

(25) Pearson, R. G. Absolute electronegativity and hardness correlated with molecular orbital theory. *Proc. Natl. Acad. Sci. U. S. A.* **1986**, *83* (22), 8440−8441.

(26) Weinhold, F.; Landis, C. R. *Valency and bonding: a natural bond orbital donor-acceptor perspective*; Cambridge University Press, 2005.

(27) Zhan, C.-G.; Nichols, J. A.; Dixon, D. A. Ionization potential, electron affinity, electronegativity, hardness, and electron excitation energy: molecular properties from density functional theory orbital energies. *J. Phys. Chem. A* **2003**, *107* (20), 4184−4195.

(28) Perdew, J. P.; Levy, M. Comment on "Significance of the highest occupied Kohn-Sham eigenvalue". *Phys. Rev. B* **1997**, *56* (24), 16021.

(29) Parr, R. G.; Szentpály, L. v.; Liu, S. Electrophilicity index. *J. Am. Chem. Soc.* **1999**, *121* (9), 1922−1924.
(30) Yossa Kamsi, R. A.; Ejuh, G. W.; Tadjouteu Assatse, Y.; Njeumen, C. A.; Tchoffo, F.; Ndjaka, J. M. B. Computational study of reactivity and solubility of Rubescin D and E molecules in gas phase and in solvent media using Hartree-Fock and DFT methods. *Chin. J. Phys.* **2019**, *60*, 1−11.
(31) (a) Taylor, R. D.; Jewsbury, P. J.; Essex, J. W. A review of protein-small molecule docking methods. *J. Comput.-Aided Mol. Des.* **2002**, *16* (3), 151−166. (b) Meng, X.-Y.; Zhang, H.-X.; Mezei, M.; Cui, M. Molecular docking: a powerful approach for structure-based drug discovery. *Curr. Comput.-Aided Drug Des.* **2011**, *7* (2), 146−157. (c) Salmaso, V.; Moro, S. Bridging molecular docking to molecular dynamics in exploring ligand-protein recognition process: An overview. *Front. Pharmacol.* **2018**, *9*, 923.
(32) Trott, O.; Olson, A. J. AutoDock Vina: improving the speed and accuracy of docking with a new scoring function, efficient optimization, and multithreading. *J. Comput. Chem.* **2010**, *31* (2), 455−461.
(33) Kannan, K.; Ramanadham, M.; Jones, T. Structure, refinement, and function of carbonic anhydrase isozymes: refinement of human carbonic anhydrase I. *Ann. N.Y. Acad. Sci.* **1984**, *429*, 49−60.
(34) Mahmudov, I.; Demir, Y.; Sert, Y.; Abdullayev, Y.; Sujayev, A.; Alwasel, S. H.; Gulcin, I. Synthesis and inhibition profiles of N-benzyl- and N-allyl aniline derivatives against carbonic anhydrase and acetylcholinesterase−A molecular docking study. *Arabian J. Chem.* **2022**, *15* (3), 103645.
(35) Ivanova, J.; Leitans, J.; Tanc, M.; Kazaks, A.; Zalubovskis, R.; Supuran, C. T.; Tars, K. X-ray crystallography-promoted drug design of carbonic anhydrase inhibitors. *Chem. Commun.* **2015**, *51* (33), 7108−7111.
(36) Kryger, G.; Silman, I.; Sussman, J. L. Structure of acetylcholinesterase complexed with E2020 (Aricept®): implications for the design of new anti-Alzheimer drugs. *Structure* **1999**, *7* (3), 297−307.
(37) https://www.rcsb.org/. (accessed.
(38) http://www.3dsbiovia.com/. (accessed on September 10, 2025).
(39) (a) Ritchie, T. J.; Macdonald, S. J. How drug-like are 'ugly' drugs: do drug-likeness metrics predict ADME behaviour in humans? *Drug Discovery Today* **2014**, *19* (4), 489−495. (b) Jia, C.-Y.; Li, J.-Y.; Hao, G.-F.; Yang, G.-F. A drug-likeness toolbox facilitates ADMET study in drug discovery. *Drug Discovery Today* **2020**, *25* (1), 248−258. (c) Ursu, O.; Rayan, A.; Goldblum, A.; Oprea, T. I. Understanding drug-likeness. *WIREs Comput. Mol. Sci.* **2011**, *1* (5), 760−781.
(40) Daina, A.; Michielin, O.; Zoete, V. SwissADME: a free web tool to evaluate pharmacokinetics, drug-likeness and medicinal chemistry friendliness of small molecules. *Sci. Rep.* **2017**, *7* (1), 42717.
(41) Lipinski, C. A.; Lombardo, F.; Dominy, B. W.; Feeney, P. J. Experimental and computational approaches to estimate solubility and permeability in drug discovery and development settings. *Adv. Drug Delivery Rev.* **1997**, *23* (1−3), 3−25.
(42) Verpoorte, J. A.; Mehta, S.; Edsall, J. T. Esterase activities of human carbonic anhydrases B and C. *J. Biol. Chem.* **1967**, *242* (18), 4221−4229.
(43) Ellman, G. L.; Courtney, K. D.; Andres Jr, V.; Featherstone, R. M. A new and rapid colorimetric determination of acetylcholinesterase activity. *Biochem. Pharmacol.* **1961**, *7* (2), 88−95.



https://doi.org/10.1021/acsomega.6c01815
ACS Omega XXXX, XXX, XXX−XXX